Thin–Walled Structures 216 (2025) 113646

Contents lists available at ScienceDirect

Thin-Walled Structures

journal homepage: www.elsevier.com/locate/tws

Experimental and numerical investigation on seismic performance and yielding sequence of coupled-double skin composite walls

Haowen Hou [a,b,c], Wei Wang [a,b,*], M. Shahria Alam [c], Shiye Wang [a,b], Jiajun Du [a,b]

[a] State Key Laboratory of Disaster Reduction in Civil Engineering, Tongji University, Shanghai 200092, China
[b] Shanghai Engineering Research Center for Resilient Cities and Intelligent Disaster Mitigation, Shanghai, 200092, China
[c] School of Engineering, The University of British Columbia, Kelowna, BC V1V 1V7, Canada

ARTICLE INFO

Keywords:
Double-skin composite wall
Coupled walls
Coupling ratio
Experimental and numerical study

ABSTRACT

The coupled double skin composite wall (C-DSCW) system is a special type of lateral force-resisting structure that consists of innovative double skin composite walls (DSCWs) and steel coupling beams. To further investigate the seismic performance and damage sequence of the C-DSCW system, an experimental study is conducted on a 3-story C-DSCW specimen under combined axial compression and horizontal cyclic loading. The test results validate the recoverability and seismic resilience of the C-DSCW system with replaceable steel coupling beams. The test also highlights the superior ductility and energy dissipation capacity of a properly designed C-DSCW system. Based on the experimental results, the modeling method of the novel C-DSCW system is developed and validated. A parametric analysis is conducted and the analytical results show that the coupling ratio, axial compression ratio, and structural aspect ratio are the key factors influencing the yielding sequence of the coupling beams and DSCWs. The value of the coupling ratio should be prioritized to ensure a reasonable yielding sequence for the C-DSCW system, based on which a higher coupling ratio value is recommended to be employed to fully utilize the coupling effect. Additionally, a quantitative relationship between the structural parameters and the recommended values of the coupling ratio is also provided.

1. Introduction

Shear wall structures are extensively employed in residential and public buildings due to their considerable lateral stiffness, strength, and ability to control horizontal drifts. Due to the architectural requirements for doors and windows, entire shear walls are often segmented by openings, resulting in multiple smaller, independent wall piers connected by coupling beams. The deformation of the coupling beams is compatible with that of the shear walls connected on both sides. This mechanism, as shown in Fig. 1, enables the coupling beams to transfer vertical forces between adjacent walls, which creates a frame-like coupling action that resists a portion of the total overturning moment induced by lateral loads [1–3].

The additional vertical tensile and compressive forces in the wall piers form an anti-overturning force couple that can reduce the moments originally resisted by the individual wall piers, resulting in higher structural efficiency. The coupling beams also provide a means of dissipating earthquake energy throughout the height of the structure as they undergo inelastic deformations, extending the energy dissipation beyond the walls' limited plastic hinge regions. From a global perspective, the coupling beams enhance the integrity between the wall piers, allowing coupled wall systems to combine considerable lateral resistance and high ductility. That is, the coupled wall system exhibits lateral stiffness and load-bearing capacity that is significantly greater than the simple sum of the individual wall piers [4–6].

Under the action of lateral load, the resistance of the coupled wall system to overturning moments consists of two contributions. The first is the tensile and compressive force couple, i.e. coupling moment, generated by the shear forces of all the coupling beams along the height. The second is the bending moments at the bottom of the wall piers. The proportion of the coupling moment to the total anti-overturning moment is defined as the coupling ratio. Take the two-wall-pier coupled wall as an example, the CR can be calculated by Eq. (1), where L_w refers to the distance between the centroid axis of the wall piers, T refers to the axial force generated by the coupling beams, V_i refers to the shear force response in the coupling beam at the ith story, n_F refers to the number of stories, M_c and M_t refer to the moment responses in compressive and tensile wall piers, respectively.

---

* Corresponding author.
E-mail address: weiwang@tongji.edu.cn (W. Wang).

https://doi.org/10.1016/j.tws.2025.113646
Received 1 November 2024; Received in revised form 2 April 2025; Accepted 29 June 2025

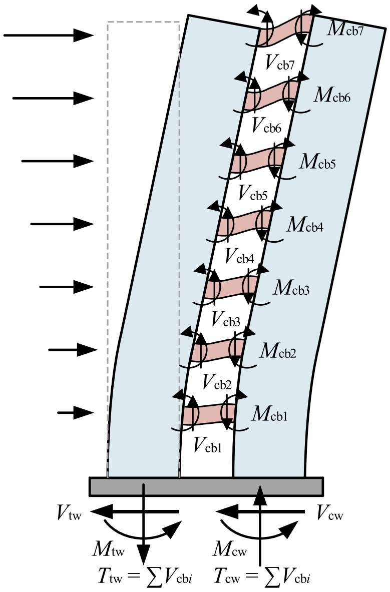

V, M, T - shear, bending, and coupling axial force responses
subscript cb$i$ - coupling beam at ith floor
subscript cw, tw - compression and tension wall pier

Fig. 1. Coupling mechanism in the coupled wall system.

$$CR = \frac{L_w T}{L_w T + M_c + M_t} = \frac{L_w \sum_{i=1}^{n_F} V_i}{L_w \sum_{i=1}^{n_F} V_i + M_c + M_t} \tag{1}$$

The CR is related to the internal force responses of the coupling beams and the wall piers. It is not a constant value due to the differences in the non-linear behaviors of these components. Fig. 2 illustrates the typical development of CR during a pushover process [1,2,7–9]. The concrete cracking leads to a reduction in stiffness of the wall piers, which decreases their moment contribution, resulting in a short rising branch in the CR curve. As the lateral load increases, the yielding of coupling beams and the strengthening of wall piers result in a decreasing branch in the CR curve. This decrease tends to stabilize as the wall piers form plastic hinges and lateral stiffness degrades.

The coupling beams are initially considered as part of the wall, and the reinforced concrete (RC) coupling beams require specialized design [10–12] to meet the deformation and internal shear force demands. However, RC coupling beams are prone to impractical design results and typically have lower performance expectations [13] due to the limited shear capacity of RC materials. Benefiting from higher shear strength, superior ductility, greater energy dissipating capacity, and more stable hysteresis properties, the steel and steel-concrete composite coupling beams are increasingly utilized in the hybrid coupled wall (HCW) system [14–16]. The application of steel coupling beams separates walls and coupling beams into two distinct functional components: the former serving as the primary structural elements and the latter acting as the energy-dissipating elements. Similar to eccentrically braced frames (EBF), the steel coupling beams are recommended to function as short shear links, dissipating energy through inelastic shear deformation [17–18]. Furthermore, based on the concept of damage control and earthquake-resilient structures [19–20], the coupling beams can be subdivided into a replaceable steel shear link serving as the structural fuse along with two non-energy dissipating beams [14,18,21–22].

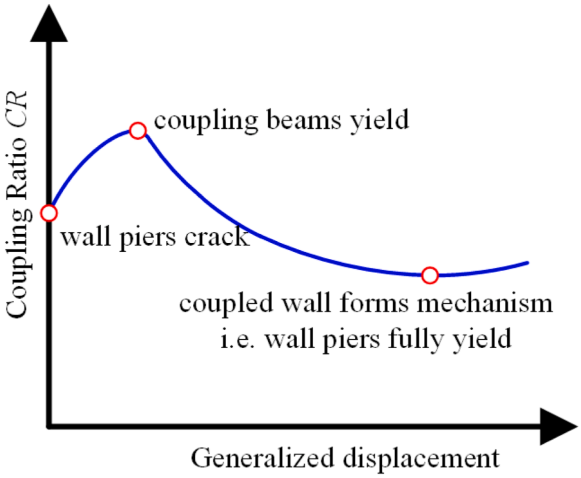

Fig. 2. Typical development of CR during a pushover process.

In addition to the innovation on coupling beams, the optimization of shear walls, such as the steel plate reinforced concrete composite walls (SPRCW) [7] and partially encased composite (PEC) shear walls [8,23], becomes essential to improve the performance of the coupled wall system. Double-skin composite shear walls (DSCWs) have gained worldwide popularity in recent years due to their advantages in convenient assembling construction, reliable seismic performance, and higher indoor space utilization [24]. The DSCWs are constructed with two steel faceplates linked by connectors, with the cavities filled with concrete. The steel faceplates provide confinement to the concrete, while the concrete provides lateral support for steel faceplates to avoid premature out-of-plane local buckling. This interaction effectively enhances the load-bearing capacity and ductility of the DSCWs [25–26]. The implementing of DSCWs contributes to damage control and seismic resilience of the coupled wall system in high seismic-intensity regions [27–28]. Additionally, the prefabricated steel plates can serve as permanent formwork for concrete casting, facilitating industrialized production and assembly in construction. Although there have been some preliminary studies and engineering applications of the coupled-double skin composite wall (C-DSCW) system [29–32], the implications of employing DSCWs in the coupled wall system on the mechanical properties require further investigation.

In this study, a 3-story C-DSCW specimen is tested under combined axial compression and horizontal cyclic loading. The steel coupling beam is designed as a replaceable shear link together with two elastic connecting beams. The tested results validate the recoverability and resilience of the C-DSCW system by replacing the shear links. Based on the tested results, the finite element model (FEM) is established and validated by the OpenSEES platform. The definition of the nominal plastic coupling ratio CR_{pn} is proposed to address the limitations of elastic and plastic coupling ratios (CR_e and CR_p). Parametric analysis reveals that the CR_{pn}, axial compression ratio (n), and structural aspect ratio (λ) are the key factors influencing the yielding sequence of the shear links and DSCW piers. The results emphasize that the CR_{pn} is the most critical design parameter in the coupled wall system and has interactive influences with other structural parameters. CR_{pn} should be controlled in a suitable range to ensure a reasonable yielding sequence. Meanwhile, higher CR_{pn} value is also recommended to fully utilize the coupling effect. Additionally, a quantitative relationship between the structural parameters and the recommended values of the CR_{pn} is also provided.

2. Experimental program

2.1. Details of the tested C-DSCW specimen

The tested specimen is extracted from a typical I-shaped coupled wall in the first standard floor of a prototype structure. Due to the laboratory limitations, the coupled wall specimen is redesigned and fabricated as an approximately 1/2 scaled specimen. The details of the scaled DSCW piers are designed following design codes [33–35]. Since the DSCW piers are scaled and the number of stories of the test specimen is less than the actual structure, the dimensions of shear links and elastic connecting beams are redesigned based on CR_{pn} to match the tested DSCW piers. Detailed information on the representative values of coupling ratio is provided in Section 4.2.

The cross-sectional dimension of the DSCW piers is 640 × 80 mm (length × width), with a thickness of 4 mm for steel plates and interior rib connectors. The interior rib connectors divide the DSCW body into five cavities, each approximately 96 mm in length. The square steel tubes are arranged on both ends of the DSCW cross-section with side lengths of 80 mm. The height of the DSCWs from the bottom plate to the top plate is 3660 mm. Triangular stiffeners with a side length of 120 mm are provided at the bottom of the DSCWs to release stress concentration and to construct the ideal fixed connection at the base of the specimen.

The shear links and elastic connecting beams are H-shaped built-up sections fabricated by welding. The shear links are designed according to the code ANSI/AISC 360 [34] with a cross-sectional dimension of 160 × 80 × 8 × 6 mm (height × width × flange thickness × web thickness), and the length, i.e., the shear span, is 244 mm. The configuration of the elastic connecting beams is following Ref., [36], with the cross-sectional dimension 300 × 100 × 10 × 8 mm (height × width × flange thickness × web thickness). The length of the elastic connecting beams exposed outside the DSCWs is 100 mm and the insertion depth is 50 mm, semi-circular holes with 52 mm diameter are set on their inserted flanges to avoid obstructing the concrete pouring. Short stiffeners with the same thickness as the webs are provided on the webs of shear links and elastic connecting beams to avoid shear buckling and local compressive buckling. The dimension of the end plates is 300 × 100 × 14 mm (height × width × thickness). Eight M16 slip-critical high-stress bolts are employed in the end plate connections to maintain the bolted connections elastic without slipping, as verified during the test process. The geometries and dimensions are shown in Figs. 3 and 4.

2.2. *Material properties*

The tested material properties of the key steel parts are listed in Fig. A1 and Table 1. The steel coupon tensile tests are conducted following the procedure in [37]. Considering the narrow internal dimension of the DSCW cross-section, special fine-aggregate concrete is employed for the concrete. The compressive strength of concrete cubic specimens with a side length of 150 mm are tested and the average strength $f_{\mathrm{c,cube}}$ value is 47.0 MPa. Considering the effective working condition of concrete in DSCWs is mainly axial compression, the formula in Ref., [38] is employed to transfer the $f_{\mathrm{c,cube}}$ into the cylinder compressive strength f_{c}'=39.3 MPa, as shown in Eq. (2). Derived from the tested material properties, the nominal plastic coupling ratio CR_{pn} for the C-DSCW specimen is 0.37, the cross-sectional pure bending

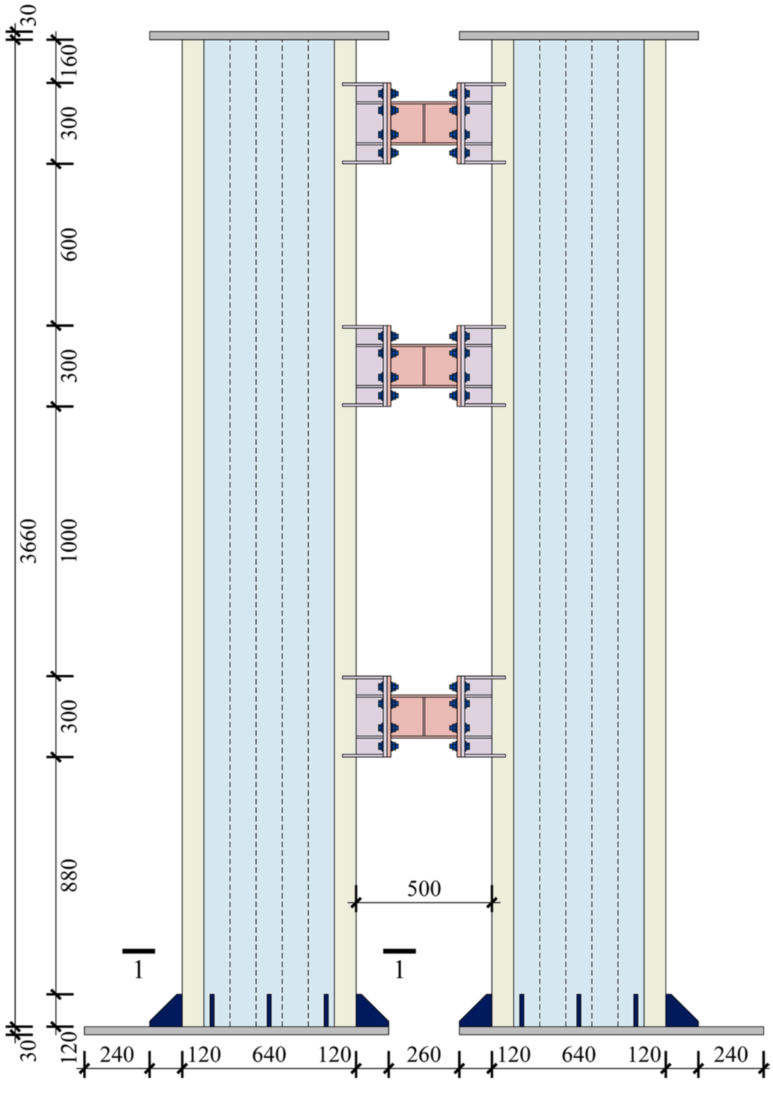

Fig. 3. Overall dimensions of the C-DSCW specimen.

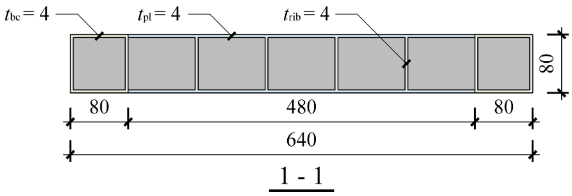

(a) DSCW pier

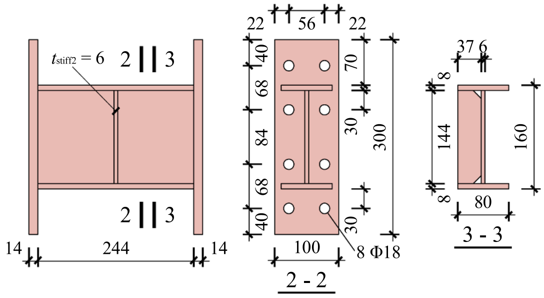

(b) Shear link

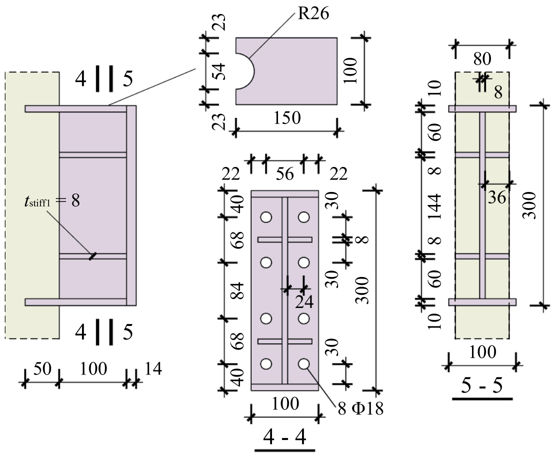

(c) Elastic connecting beam

Fig. 4. Dimensions and constructional details of the members in C-DSCW specimen.

strength of one DSCW pier is M_{pn}=613.4 kN•m.

$$f'_c = \left[0.76 + 0.2\log_{10}\left(\frac{f_{cu}}{19.59}\right)\right] f_{cu} \quad (\text{unit}: \text{MPa}) \tag{2}$$

2.3. Test setup and loading protocol

2.3.1. Test setup

The test is conducted at the Structural Laboratory of Tongji University with the test setup depicted in Fig. 5. Each DSCW pier is fixed to the steel base with ten M36 high-strength bolts. The DSCW-to-base connection is checked to remain elastic without local deformation during the cyclic loading. The steel base is fastened to the ground by several anchor bolts. Since the test equipment system has only one vertical servo actuator, a two-level loading beam system is designed to apply the vertical load uniformly on the two DSCW piers. On the top end plate of each DSCW pier, a second-level loading beam with a semi-circular groove is fixed using high-strength bolts. The first-level loading beam is connected to the vertical actuator and is equipped with two convex arcs at the bottom of the lower flange. The convex arc has a smaller radius (radius 60 mm) than that of the semi-circular groove (radius 150 mm) and extends far enough to ensure rotation space. The Teflon plates are installed at the arc-groove interface to minimize frictional constraints on DSCW deformation.

The horizontal loading point is positioned at the height of the centerline of the shear link on the third story. Excluding the height of the bottom stiffeners, the effective horizontal loading height is H_e = 3230 mm. The horizontal loading device comprises two horizontal loading bases, two steel support plates, and two long high-strength anchors. The two horizontal loading bases are placed on either outer side of the two DSCWs and linked by two long anchors. The steel support plates are welded on the DSCWs to support the horizontal loading bases. The horizontal servo actuator is connected to one horizontal loading base with a steel pin. The horizontal loading device enables the C-DSCW system to always be subjected to pushing action during cyclic loading to avoid localized tensile damage. On both the front and back faces of each DSCW pier, lateral supports are installed to prevent out-of-plane global deformation. The lateral supports are contacted to the DSCWs by lubricated spherical bearings to minimize frictional constraints on DSCW deformation.

2.3.2. Loading protocol

The C-DSCW specimen is tested under combined axial compression and horizontal cyclic loading. A constant axial load of 2550 kN is applied to the top of the C-DSCW system, i.e. 1275 kN on each DSCW pier, corresponding to the axial load ratio of $n = 0.29$. Eq. (3) is the expression for n, where N refers to the axial compressive force, $A_{s,bc}$ and $A_{s,ic}$ refer to the areas of one boundary steel tube and the steel plates of the DSCW body (the portion excluding the boundary columns, including the steel faceplates and interior rib connectors), $A_{c,bc}$ and $A_{c,ic}$ refer to the areas of concrete in one boundary column and the DSCW body, $f_{y,bc}$ and $f_{y,ic}$ refer to the yield strengths of the boundary steel tube and the steel faceplate of the DSCW body, f_c' refers to the cylinder compressive strength of concrete, respectively.

$$n = \frac{N}{2A_{s,bc}f_{y,bc} + A_{s,ic}f_{y,ic} + \left(2A_{c,bc} + A_{c,ic}\right)f'_c} \tag{3}$$

In the horizontal direction, the C-DSCW specimen is subjected to displacement-controlled cyclic loading according to the protocol presented in Fig. 6. The loading displacement amplitudes and the number of cycles are determined in reference to FEMA 461 [39], where the drift ratio δ is determined as $\delta = \Delta/H_e$, Δ refers to the lateral loading displacement. The experimental process is divided into two stages. The

Table 1
Steel material properties (unit: MPa).

No.	Steel type	E_s ($\times 10^5$)	f_y	f_u	σ_u	EAF (%)
T-4	Boundary steel tube of DSCW	2.31	428	557	651	32
PL-4	Steel faceplate and interior rib connector of DSCW	1.97	322	480	592	36
PL-6	Shear link web	2.10	411	541	652	34
PL-8	Shear link flange and elastic connecting beam web	2.21	430	596	706	31
PL-10	Elastic connecting beam flange	1.84	363	532	640	30
PL-14	End plate	1.88	370	534	666	28

Note: E_s refers to Young's modulus, f_y and f_u refer to the yield and ultimate strength expressed in engineering values, and σ_u refers to the logarithmic stress value at the peak point of the engineering stress-strain curve, EAF is the elongation at fracture.

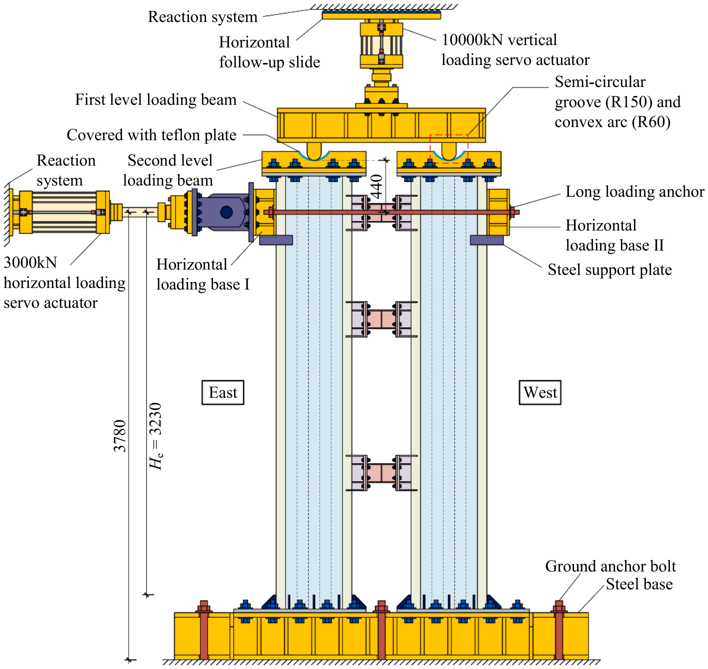

(a) Front view

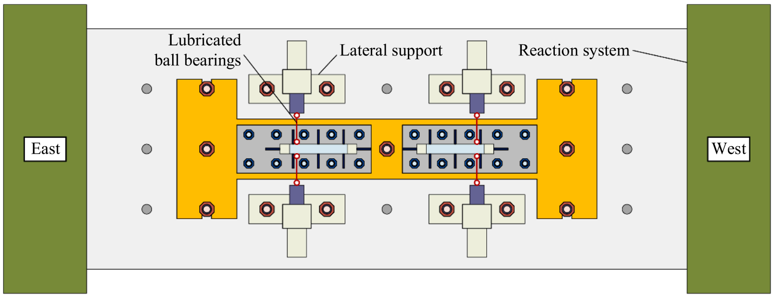

(b) Top view

Fig. 5. Test setup.

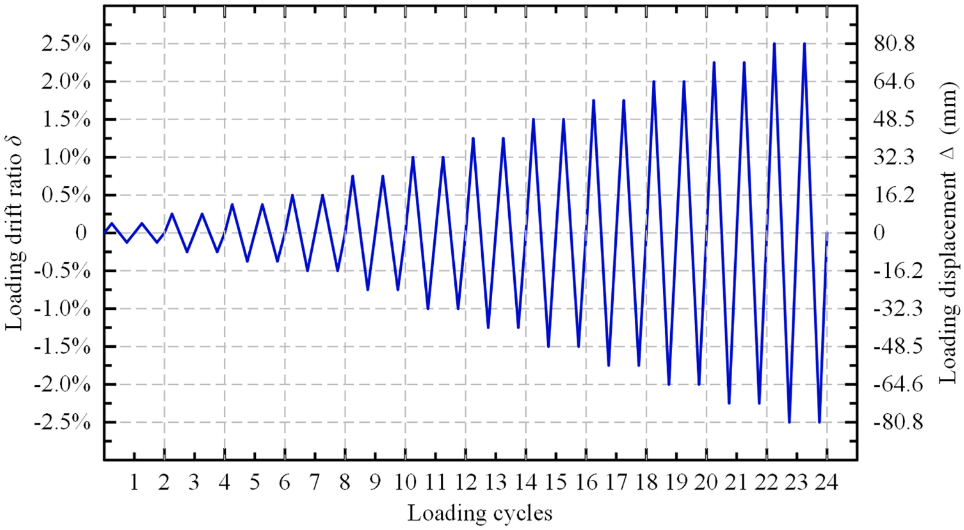

Fig. 6. Loading protocol.

first stage is loaded to a maximum displacement amplitude corresponding to drift ratio of 0.75%, after which the horizontal and axial forces are unloaded to remove and replace the damaged shear links. The second loading stage is conducted with the same loading settings as the first stage, and terminated when the lateral load reduced to below 85% of its peak value.

2.3.3. Instrumentation

The instrumentation layout is illustrated in Fig. 7. H and X denote horizontal and diagonal displacement transducers (DTs), respectively.

H1~H4 DTs are placed at the center of the two DSCW piers at the same height as the loading point to monitor the horizontal loading displacement. H5~H8 DTs are placed according to the height of the center line of the coupling beams on the first and second stories to monitor the overall deformation pattern of the DSCW piers. X1~X4 and X5~X10 DTs are placed at the bottom story of DSCW piers and on the shear links respectively to monitor the shear deformation. S and T refer to unidirectional and triaxial strain gauges (SGs), respectively, with subscripts indicating the monitored component. $T_W1 \sim T_W18$ and $S_W1 \sim S_W44$ SGs are placed bottom-up on several cross-sections spacing 100 mm apart from the bottom of the DSCWs. $T_{CB}1 \sim T_{CB}6$ and $S_{CB}1 \sim S_{CB}12$ SGs are placed on the webs and flanges of the shear links, respectively. $T_C1 \sim T_C3$ and $S_{ECB}1 \sim S_{ECB}2$ SGs are used to verify the elastic behaviors during the test of the elastic connecting beams and the beam-to-DSCW connections.

3. Experimental results and discussion

3.1. Damage progression and failure mechanism

3.1.1. The first loading stage

During the first four loading levels, i.e., up to the 0.5% drift ratio, the DSCW piers remain elastic and the shear links at the second and third stories sequentially exhibit web yielding according to the monitoring results. During the 0.5% drift ratio loading, the bottom of the west DSCW pier near the neutral axis exhibits a hollow sound when tapped with a rubber mallet, but no local buckling is detected through visual and tactile inspections. During the 0.75% drift ratio loading, slight local buckling that could only be detected by touch appeared on the west DSCW pier. Obvious shear deformation of the shear links can be observed through the mesh drawn on their webs. The first loading stage stopps after the 0.75% drift ratio, and the shear links are removed and replaced after the horizontal force is unloaded. The residual deformations of the removed shear links are within 0.25% shear drift ratio, which is less than the maximum allowable shear drift ratio of 0.4% of the replaceable shear links [22,40]. Fig. 8 displays the tested phenomena in the first loading stage.

3.1.2. The second loading stage

The tested phenomena of the second loading stage remain essentially the same as those experienced in the first loading stage up to 0.75% drift ratio. During the first positive cycle of the 1.0% drift ratio loading, the front faceplate of the west DSCW pier shows visible local buckling. During the second negative cycle of the 1.25% drift ratio loading, several bulges also appear on the front faceplate of the east DSCW body. The peeling of white paint at the outer corners of the DSCW piers indicates that plastic strain concentrates in these areas. During the 1.5% drift ratio loading, these bulges expand horizontally, and the local buckling also appears at the bottom of the two outer boundary columns. During the 1.75% drift ratio loading, the local buckling expands throughout the west DSCW body, and a minor fracture is observed on the outer boundary column of this DSCW pier. The white paint at the inner corners of the C-DSCW specimen begins to peel off. Meanwhile, the load-displacement curve of C-DSCW begins to show degradation. During the first negative cycle of the 2.0% drift ratio loading, the local buckling expands throughout the east DSCW body, and the fracture extends across the width of the outer boundary column of the west DSCW pier. As reversing the loading direction, a fracture is also observed on the outer boundary column of the east DSCW pier. During the 2.5% drift ratio loading, the fracture penetrates through the faceplate of the boundary column and one cavity of the wall body, leading to the termination of test due to severe damage. Fig. 9 displays the tested phenomena in the second loading stage.

3.2. Seismic performance

3.2.1. Load-displacement curves

The load-displacement hysteresis curves are obtained by the average readings of H1~H4 DTs, as shown in Fig. 10. The red and black lines represent the first and second loading stages, respectively. The curve of the first loading stage shows relatively full energy dissipation hysteresis loops which closely resembles the second loading stage. This indicates that the shear links have already undergone shear yielding and effectively dissipated energy. The damage is confined to the shear links within 0.75% drift ratio, and the seismic performance of the C-DSCW system can be restored to an intact state by replacing the shear links. The entire hysteresis loops of the second loading stage exhibits a stable response, showing no pinching is observed and demonstrating effective

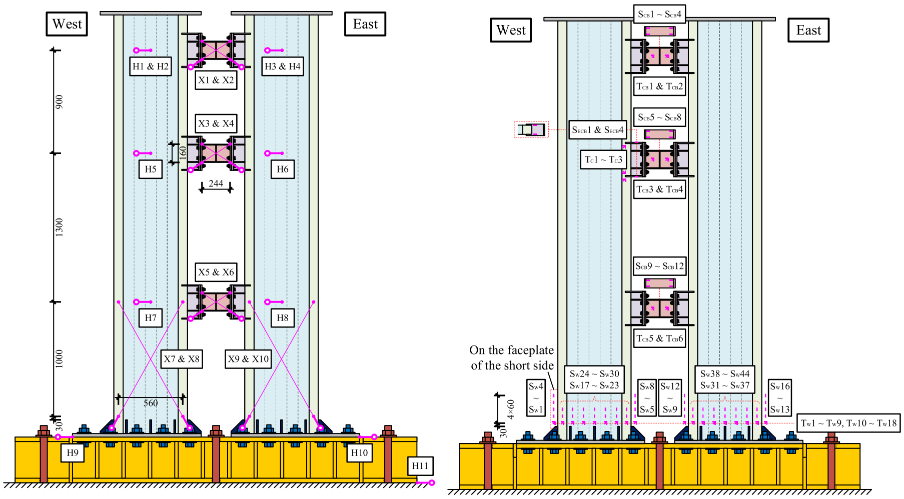

(a) Displacement transducers (DTs)
(b) Strain gauges (SGs)

Fig. 7. Arrangement of the instrumentation.

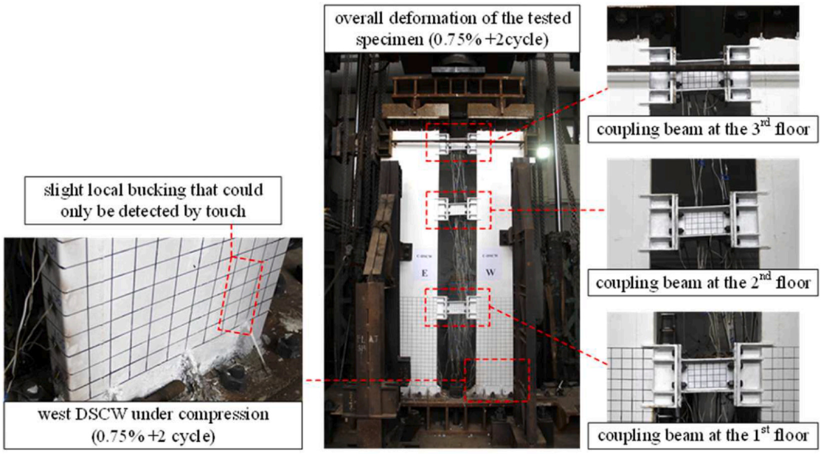

(a) 0.75% drift ratio

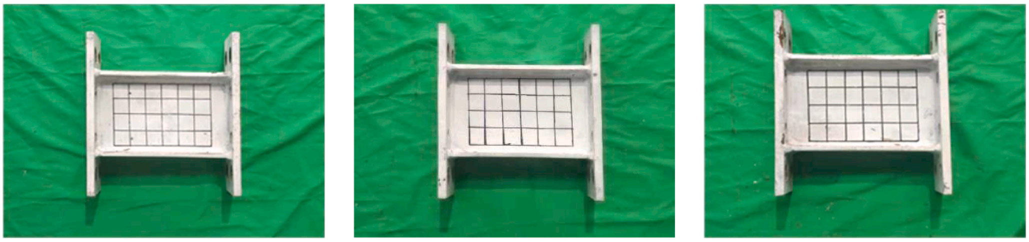

(b) Residual deformation of the shear links at the 1st, 2nd, and 3rd stoies

Fig. 8. Photographs of the first loading stage.

energy dissipating capacity.

3.2.2. Ductility, energy dissipation capacity, and stiffness degradation

The skeleton curve of the second loading stage is extracted as shown in Fig. 11. The displacement ductility coefficient μ is defined as the ratio of the ultimate displacement (Δ_u) to the yield displacement (Δ_y). As illustrated in Fig. 12, the yield point is determined by the farthest point method [41], and the ultimate point is identified where the load is reduced to 85% of its peak value. The farthest point method is to find the intersection point (tangent point) on the rising branch of the generalized load-displacement curve with the furthest distance from the parallel line connecting the peak point with the origin. The energy dissipation capacity is evaluated by the cumulative energy (E) and equivalent damping ratio (ζ_{eq}). The equivalent damping ratio ζ_{eq} can be determined by Eq. (4), where S_{ABC} is the area enclosed by curve ABC as shown in Fig. 13. Similar definitions are applied to S_{CDA}, S_{OBE}, and S_{ODF}. The cumulative dissipated energy and equivalent damping ratio are shown in Fig. 14(a) and (b), respectively. All of the indexes and the characteristic points of the skeleton are summarized in Table 2.

$$\zeta_{eq} = \frac{S_{ABC} + S_{CDA}}{2\pi(S_{OBE} + S_{ODF})} \tag{4}$$

The secant stiffness ratio (ξ) can provide a quantitative measure of stiffness degradation and is defined as K_i/K_1, where K_i can be calculated using Eq. (5), representing the secant stiffness of the ith complete cycle, K_1 refers to the stiffness of the first loop. F_i and -F_i refer to the positive and negative peak load values of the ith complete cycle, Δ_i and -Δ_i refer to the corresponding displacements, respectively. Fig. 15 presents the stiffness degradation of the C-DSCW specimen. The secant stiffness declines rapidly within the 0.5% loading due to the yielding of the shear links. After that, the degradation rate of secant stiffness decreases, and there is no abrupt drop in secant stiffness curves even the buckling and fracture occur.

$$K_i = \frac{|F_i| + |-F_i|}{|\Delta_i| + |-\Delta_i|} \tag{5}$$

3.3. Strain responses

A detailed analysis of the strain responses on the DSCW piers and shear links can further reveal the force mechanisms and the plasticity evolution of the C-DSCW system. The horizontal strain responses recorded by the triaxial strain gauges in the bottom section of the DSCW piers remain consistently within a small range before the local buckling becomes significant and distorts the strain reading. Consequently, the cross-sectional strain responses of the DSCW piers are displayed by the vertical strain gauges, as shown in Fig. 16. This behavior aligns with the force characteristics typical of flexure-controlled slender shear walls.

The webs of the shear links initially yield at 0.25% loading drift ratio. Subsequently, the equivalent strain accumulates rapidly, indicating that the plasticity of the shear links is fully developed. The outer corners of the DSCW piers exhibit preliminary yielding at 0.75% loading drift ratio, while the cross-sections at the height corresponding to the S2 strain gauge remain elastic. The cross-sectional strain responses of the DSCW piers follow the plane-section assumption perfectly. The neutral axes of both DSCW piers tend to shift inward, which is the result of the combined effect of steel plates local buckling and coupling-effect-induced additional axial force. The cross-sectional strain responses of the second loading stage are basically the same as the first loading stage within 0.75% loading drift ratio. The bottom sections of the DSCW piers have fully yielded at the loading drift ratio of 1.25%, after which the bottom strain gauges are damaged. Throughout the second loading stage, the strain responses of the sections at the height corresponding to the S4 strain gauge remain elastic. This indicates that the non-linear behaviors of the DSCW piers are concentrated in the plastic hinge regions at the bottom of the walls. The range of the plastic hinge region is up to the height of approximately 210~270 mm from the bottom, which is

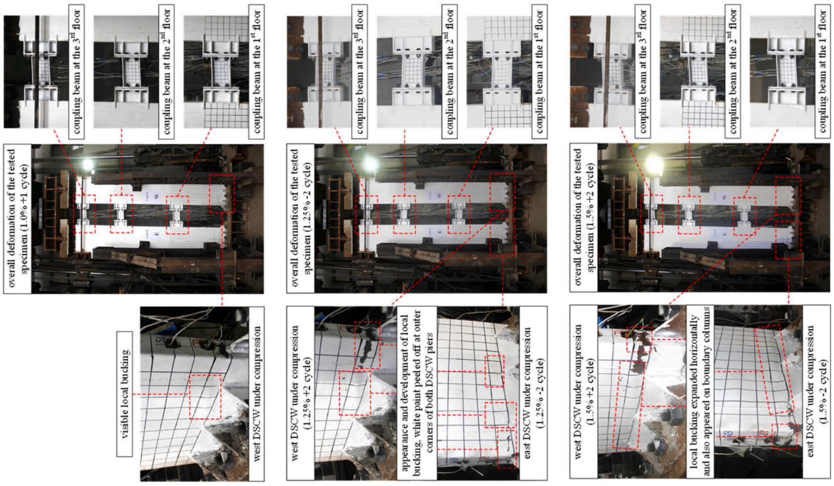

(a) 1.0% drift ratio (b) 1.25% drift ratio (c) 1.5% drift ratio

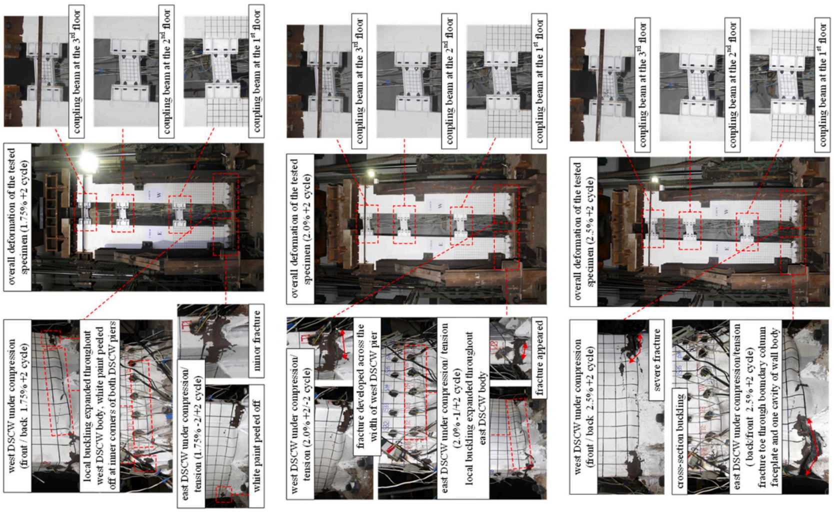

(d) 1.75% drift ratio (e) 2.0% drift ratio (f) 2.5% drift ratio

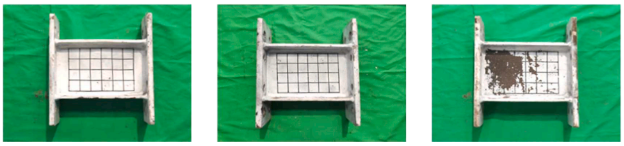

(g) Residual deformation of the shear links at the 1st, 2nd, and 3rd stories

Fig. 9. Photographs of the second loading stage.

consistent with the conclusions in [25–26,42–43], i.e., about 0.4 times the length of the DSCW cross-section.

3.4. Deformation pattern of DSCWs and shear links

The overall deformation pattern of the DSCW piers is obtained by the horizontal DTs placed at each story, as shown in Fig. 17, where the lateral drift is determined by averaging the measurements from the two DSCW piers. It is observed that the deformation pattern of the DSCWs is similar to that of a flexural cantilever beam in the elastic and early plastic stages. As the lateral loading drift increases, the deformation pattern evolves toward a straight line. This behavior indicates that once the plasticity at the bottom of the DSCW pier is fully developed, the deformation pattern of the upper wall transitions to resemble a rod rotating around the bottom plastic hinge.

The shear deformations are obtained by the diagonal DTs, and the shear drift ratio γ can be calculated by Fig. 18 and Eq. (6), where l_a and l_b are the initial side lengths of the measured region, l_1, l_2, l_1' and l_2' are the initial and measured reasdings of the two diagonal DTs, l_{v1} and l_{v2} are the changes in readings of the two diagonal DTs, respectively.

$$\gamma = \frac{\sqrt{l_a^2 + l_b^2}}{2 l_a l_b}(l_{v1} + l_{v2}) \tag{6}$$

Figs. 19 and 20 present the deformation responses of the DSCW piers and the shear links in the C-DSCW system, respectively. The diagonal DTs used to measure the shear deformation of the DSCW piers are only installed in the first story. Given the triaxial strain gauges on the DSCW piers, except for the vertical strain branches that related to flexural deformation, exhibit negligible responses, it can be concluded that the shear deformation of the DSCWs remains elastic. Based on this observation, it is reasonable to assume that the DSCW piers should maintain a constant shear drift ratio along their height. Consequently, the shear deformations in the second and third floors are extrapolated by multiplying their corresponding heights (heights at DTs H5~H6, and H1~H4) by the shear drift ratio measured in the first story. It is observed in Fig. 19 that the shear deformation of the walls contributes very little

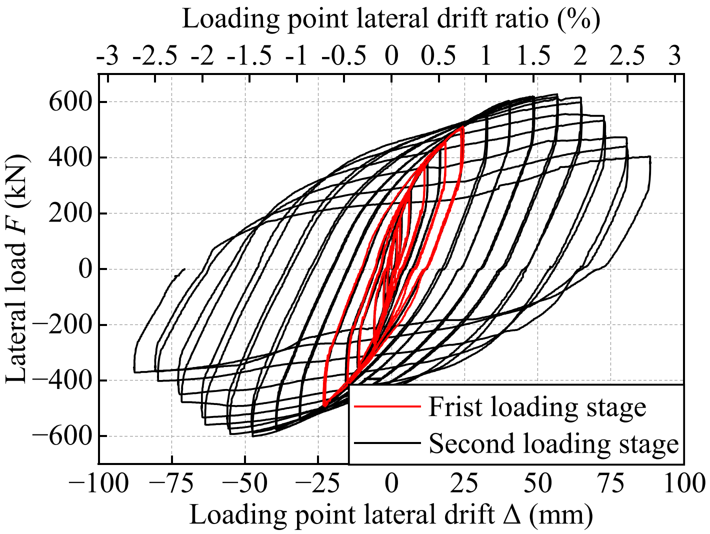

Fig. 10. Hysteresis curves.

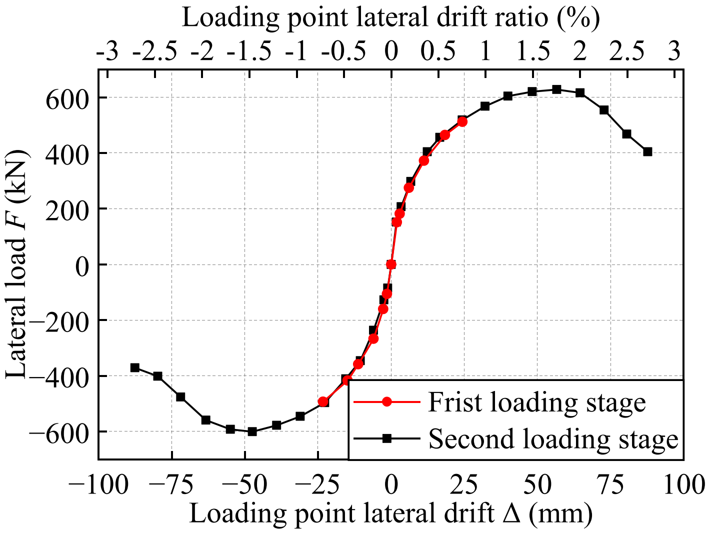

Fig. 11. Skeleton curves.

to the lateral drift at each story. Essentially, from the perspective of discretized "structural stories", the components of lateral drift in a shear wall comprise 5 parts, as illustrated in Fig. 21. For a specific structural story, the force-induced lateral displacement consists of only part 3 and part 5. This deformation is not a significant part of the total lateral drift (especially in the upper stories), but is considered to be the really "harmful" portion of deformation for the shear wall [44–45].

The shear links undergo substantial inelastic shear deformation and energy dissipation prior to C-DSCW specimen failure. The deformation amplitudes of the shear links on the second and third stories are approximately the same, while smaller on the first story. This observation reveals that the deformation of the shear links in the coupled wall system is related to the absolute drift of the wall piers. Specifically, it pertains to the global rotation of the wall section at the height where the coupling beams are located, instead of the force-induced curvature of the wall. This observation also reflects the "multi-seismic-defense" mechanism of the coupled wall system: the coupling beams are capable of fully dissipating the seismic energy throughout the entire height of the system, while the upper walls experience only limited harmful deformation.

4. Numerical analysis

4.1. Modeling method and validation

This section provides a brief introduction to the C-DSCW FEM developed by OpenSEES [46]. The DSCW piers are developed by the fiber-based beam-column elements given they are governed by flexural deformation. The modeling method in this study explicitly accounts for two critical non-linear mechanisms through specialized uniaxial material models, as shown in Fig. 22(a) and (b): (1) Beyond conventional elastoplastic behavior of steel material, the local buckling and ductile

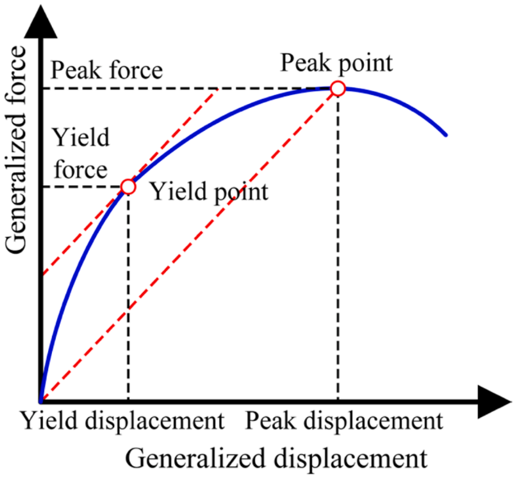

Fig. 12. Farthest point method for yield point.

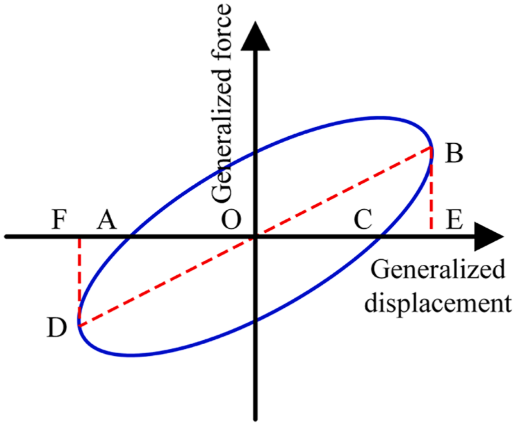

Fig. 13. Calculation of ζ_{eq}.

fracture behaviors of the external steel faceplates are captured by employing the Reinforcing Steel Material Model (RSMM) [47]. (2) The strength enhancement and ductility improvement of infilled confined concrete is considered by the Mander's confinement theory [48] together with Concrete02 material model.

Given the steel buckling and fracture predominantly localize within the wall footing, the DSCW model is partitioned into two parts to optimize computational efficiency and prevent overfitting of non-existing steel failure behaviors, as shown in Fig. 23. The special non-linear region consists of one element that extends from the wall base over a length of twice the DSCW cross-sectional width [49]. The RSMM is exclusively applied to the steel faceplate fibers in this region. The steel fibers in normal elastoplastic region are modeled using the general Steel02 material model. The multi-cavity interaction in DSCWs enhances concrete confinement beyond conventional concrete-filled steel tube (CFST) members, as shown in Fig. 22(c). This unique mechanism also needs to be considered in the Mander's model. Detailed information on the DSCW modeling methods and determination of parameters can be found in Refs. [27,49].

As for the coupling beams, the two-node link elements with axial, flexural, and shear three-direction springs are implemented for the shear links. The axial spring and flexural spring can be considered elastic, while the shear spring exhibits non-linear behaviors. The properties and calculation methods of the springs within the link elements are listed in Table 3, where E_{CB} and G_{CB} refer to Young's modulus and shear modulus of the steel of the shear link, e refers to the shear span, A_{CB} and A_w refer to the cross-sectional areas of the full section and the web, $f_{y,w}$ refers to the yield strength of the web steel plate, I_f refers to the cross-sectional moment of inertia, respectively.

The hysteresis behaviors of the non-linear shear spring is characterized by the Steel02 material model. In the Steel02 material model, the parameters R_0, cR_1, and cR_2 reflect the Bauschinger effect, the parameter b reflects the kinematic hardening effect, and the parameters a_1~a_4 represent the isotropic hardening effect, the values of these parameters are recommended in [50]. Note that the Steel02 material model is originally employed for steel members that are subject to axial or bending load, the parameter settings of the intermediate variables is unadequately suitable for shear links. Precisely, the shear-dominated hysteresis behavior exhibits the properties of the strengthening

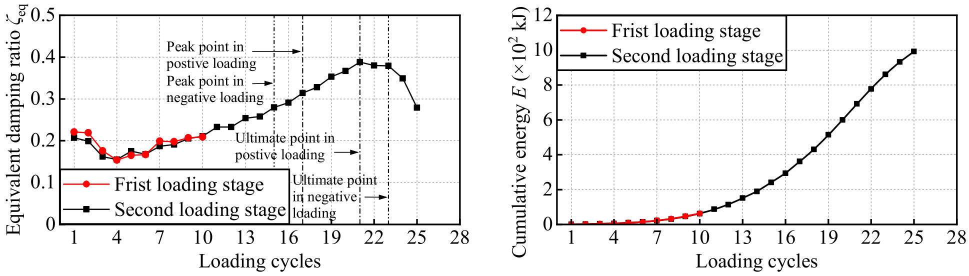

(a) Equivalent damping ratio ζ_{eq}

(b) Cumulative energy E

Fig. 14. Energy dissipation capacity.

Table 2
Characteristic points of the skeleton curve and seismic performance evaluations.

Specimen No	Loading direction	Δ_y (mm)	F_y (kN)	Δ_m (mm)	F_m (kN)	Δ_u (mm)	F_u (kN)	μ	$\overline{\mu}$	$\zeta_{eq,m}$	$\overline{\zeta}_{eq,m}$	$\zeta_{eq,u}$	$\overline{\zeta}_{eq,u}$
C-DSCW	Positive	16.7	456.1	56.6	627.8	74.6	533.6	4.48	4.44	0.314	0.297	0.379	0.384
(2nd loading stage)	Negative	15.6	411.0	47.5	601.2	68.4	511.1	4.40		0.280		0.388	

Note: Δ and F refer to the loading drift and lateral load, the subscripts y, m, and u refer to the yield, peak, and ultimate point, $\zeta_{eq,m}$ and $\zeta_{eq,u}$ refer to equivalent damping ratios at the peak point and ultimate point, $\overline{\mu}$, $\overline{\zeta}_{eq,m}$, and $\overline{\zeta}_{eq,u}$ refer to the average value of ductility coefficient and equivalent damping ratio in positive and negative loading, respectively.

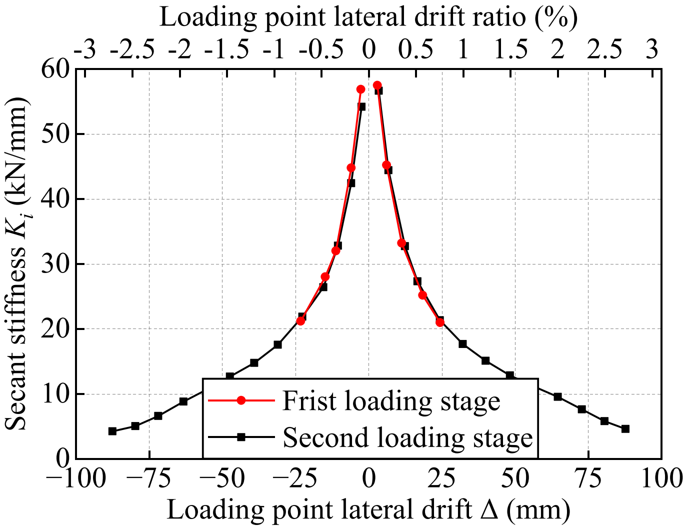

Fig. 15. Stiffness degradation.

amplitude is large in small strain ranges while moderate in large strain ranges [51–52]. To address the limitations, the power index of the intermediate variable d_1 for the isotropic hardening parameters should be revised from 0.8 to 0.6 (for low-yield-point steel material) or 0.45 (for mild steel material) [9]. Through the above methods, a new material model can be developed for the shear spring of the shear links. The elastic connecting beams are modeled by the Elastic Timoshenko Beam Column element which can accurately simulate both flexural and shear deformation of the elastic deep beams. The modeling methods for the coupling beams are specifically validated at the component level, the prototype specimens are from [21–22], and the schematic and validation results of the models are shown in Fig. 24.

To ensure the deformation compatibility between coupling beams and DSCW piers, the rigid link elements are assigned at each story of both DSCW piers, extending to their geometric boundaries, and are tied to the elastic connecting beams. Given that the end plate connections and beam-to-DSCW connections are designed as rigid connections according to [36,53], and no local deformation is observed during the test. Therefore, the mechanical behaviors of the connections are not specifically considered. The loading process involves two analytical steps. The vertical loads are first applied at the top nodes of the two DSCW piers, followed by the horizontal unit forces imposed at the third-story nodes of the two DSCW piers. The system responses are obtained through displacement-controlled analysis by proportionally scaling the horizontal unit forces until target horizontal displacements. The schematic and validation results of the modeling for the tested C-DSCW specimen are shown in Figs. 25 and 26. The simulated results are in good agreement with the tested results, the average strain responses at the DSCW bottom sections and the overall deformation pattern can also be precisely reflected, validating the computational reliability and accuracy.

4.2. Declaration of the coupling ratio

In the design process, it is essential to define an objective, specific, and constant CR as an indicator to represent the performance of the coupled wall systems. Current methodologies adopt two primary definitions: (1) The elastic coupling ratio CR_e, determined by the continuum mechanics method and the components' deformation compatibility relations under a specific lateral force distribution pattern [8,54–55]. Essentially, the CR_e represents the relative stiffness relationship between the coupling beams and the wall piers. (2) The plastic coupling ratio CR_p is defined as the coupling ratio at the system's plastic mechanism state, where all coupling beams exhibit shear yielding and both wall piers develop plastic hinges [1–2,56]. Notably, the coupling mechanism introduces additional axial tensile and compressive loads to the wall piers, which changes their plastic bending-bearing capacity. Therefore, the resisting moment of the wall piers in calculating CR_p should theoretically be determined according to the the N-M relationship [9,57–58]. However, since the bending-bearing capacity of the wall piers is not only a parameter required for CR_p calculation but also the design result controlled by CR_p, this leads to additional iterations in the design process.

To resolve this circular dependency and circumvent additional iterations in CR_p-based design process, an alternative representative coupling ratio is proposed in this study. At the critical condition that the coupling beams are all shear yielding and wall piers form plastic hinges, replacing the moment contribution of the wall piers by the cross-sectional pure bending strength M_{pn}. Define this representative CR as the "nominal plastic coupling ratio", denoted as CR_{pn}, which can be expressed by Eq. (7). Where V_{pi} refers to the plastic shear strength of the coupling beam at the ith story and can be determined by Eq. (8). For symmetrical wall piers, M_{cpn}=M_{tpn}=M_{pn}. The subscript pn indicates that the variable is related to "plastic in nominal sense". The cross-sectional pure bending strength of the DSCW piers can be derived from the force equilibrium relationship in the plastic ultimate state of the bottom section. This method has been validated by extensive experimental and numerical analysis studies [26,42,59–61]. This definition decouples CR_{pn} calculation from axial load effects, using sectional capacity as a stable reference. However, in CR_{pn}-based design practice, n needs to be considered independently, i.e., the design recommendation interval for CR_{pn} should be determined according to different axial load levels. The coupling ratios mentioned in the subsequent sections in this study all refer to CR_{pn}.

$$CR_{\mathrm{pn}} = \frac{L_{\mathrm{w}} \sum_{i=1}^{n_{\mathrm{F}}} V_{\mathrm{p}i}}{L_{\mathrm{w}} \sum_{i=1}^{n_{\mathrm{F}}} V_{\mathrm{p}i} + M_{\mathrm{c,pn}} + M_{\mathrm{t,pn}}} \Rightarrow \frac{L_{\mathrm{w}} \sum_{i=1}^{n_{\mathrm{F}}} V_{\mathrm{p}i}}{L_{\mathrm{w}} \sum_{i=1}^{n_{\mathrm{F}}} V_{\mathrm{p}i} + 2M_{\mathrm{pn}}} \tag{7}$$

$$V_{\mathrm{p}} = 0.58 f_{\mathrm{y,w}} A_{\mathrm{w}} \tag{8}$$

4.3. Parametric analysis program

Through the coupling mechanism, the coupling beams can serve as the first seismic defense to dissipate earthquake energy and to protect the wall piers, thus improving the structural ductility. In addition, the coupling beams can increase the integrity of the connected walls, which leads to higher lateral stiffness and strength. To fully utilize the coupling

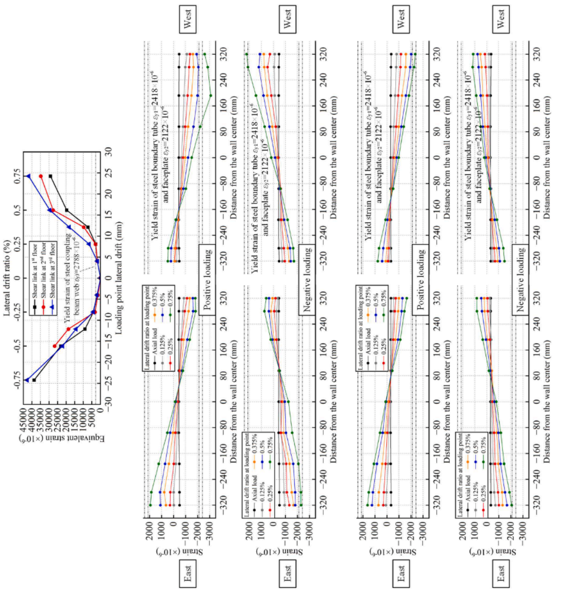

(a) Equivalent strain response envelopes of shear link webs in the first loading stage

(b) Strain response envelopes of vertical gauges of T1~T18 in the first loading stage

(c) Strain response envelopes of gauges S2, S6, S10, and S14 in the first loading stage

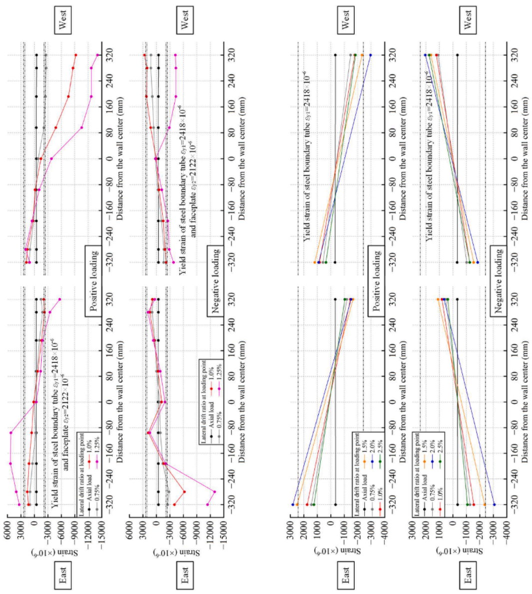

(d) Strain response envelopes of vertical gauges of T1~T18 in the second loading stage

(e) Strain response envelopes of gauges S4, S8, S12, and S16 in the second loading stage

Fig. 16. Strain responses of the DSCW piers and shear links.

effect, and also to avoid unexpected degradation of the walls' performance due to excessive additional axial forces induced by coupling moments, the shear links and walls should be designed with a reasonable yielding sequence and appropriate relative strength. Therefore, research should be conducted to reveal a reasonable range of coupling ratio values. Although the design *CR* ranges have been extensively studied for RC coupled wall systems and HCW systems, the impact of employing DSCWs in the coupled wall system on the suitable range of *CR* still requires further investigation. In this section, a parametric analysis of the C-DSCW system is carried out to investigate the effect of CR_{pn} on the yielding sequence, lateral stiffness, load-bearing capacity, etc.

The numerical models for the parametric analysis are developed based on Section 4.1, as shown in Fig. 27, where h_F refers to the story height. Two modifications are provided to make the models more realistic. One is to spread the axial load, i.e., the structural gravity, over the nodes at each story of the DSCW piers. The total axial load at the bottom section of one DSCW pier can be determined according to target axial load ratio n and Eq. (3), then uniformly distribute the total axial load to the nodes at each level of this DSCW pier.

The other is to apply the lateral force based on the first-order natural vibration mode, given that the yielding of the shear links and the preliminary plasticity development of the walls have minimal effect on the pattern of the structural natural vibration mode before the wall bottoms formed plastic hinges [62]. The lateral loading is performed by monotonic pushover, where F_{mi} refers to the normalized modal lateral force at the ith story. Additionally, a reference node is specifically identified at the top of the physical-plastic hinge region of each DSCW pier, i.e., at a height of 0.4 times the DSCW cross-sectional length from bottom, as shown in Fig. 27. By recording the response in the third displacement degree of freedom at these nodes, the rotation responses of the plastic hinge regions of the two DSCW piers can be obtained.

The cross-sectional dimension of the DSCW piers is 3600 × 160 mm (length × width), with a thickness of 4 mm for steel sheets and interior rib connectors. Twelve interior rib connectors divide the DSCW into 13 cavities, each approximately 248 mm in length. On both ends of the DSCW section are square steel tubes with side lengths of 160 mm. The steel material is assumed to be Chinese Q355 steel with a yield strength of 355 MPa, and the concrete material is assumed to be Chinese C40 with a cylinder compressive strength of 32.9 MPa. The cross-sectional pure bending strength of one DSCW pier is M_{pn}=18950 kN•m. The shear links and the elastic connecting beams have a length of 800 mm.

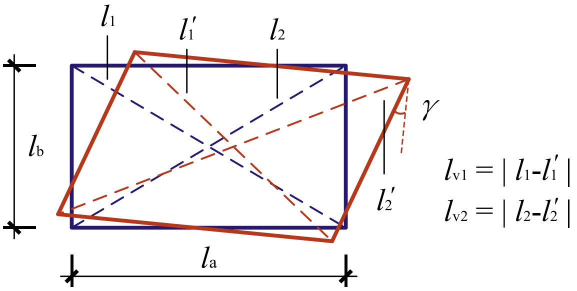

Fig. 18. Calculation of shear deformation.

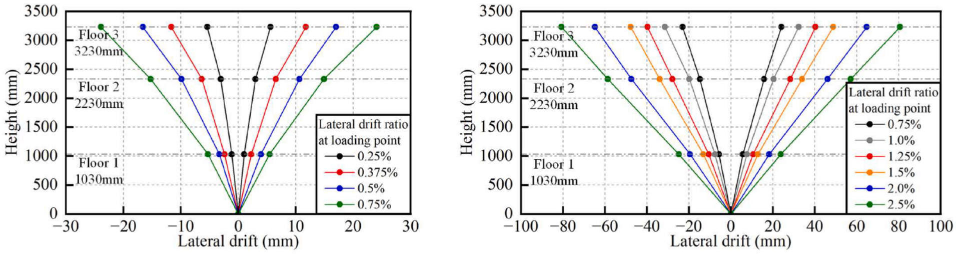

(a) Deformation pattern in the first loading stage

(b) Deformation pattern in the second loading stage

Fig. 17. Lateral deformation pattern.

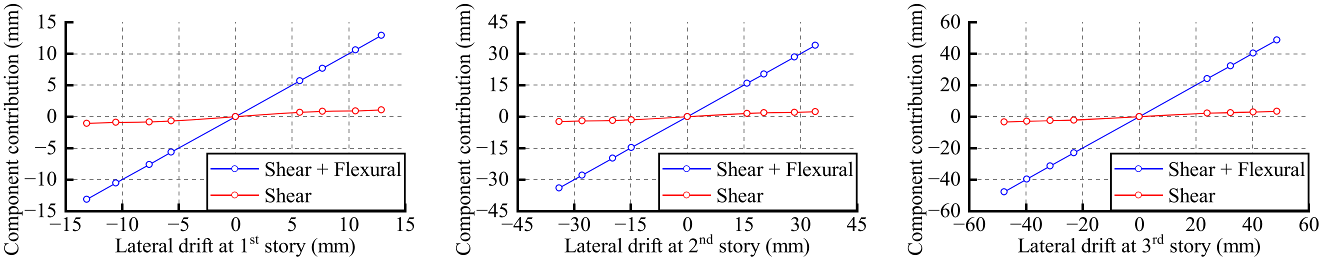

Fig. 19. Deformation contribution to the lateral drift at each story.

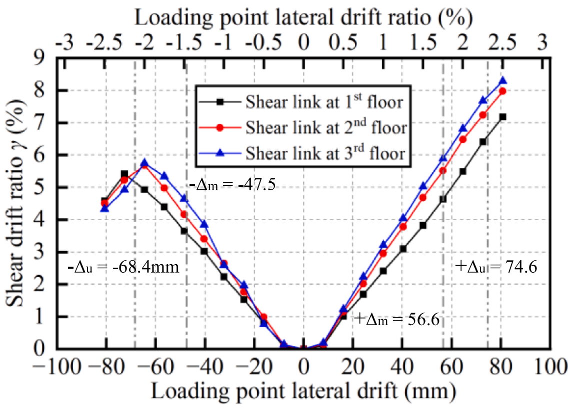

Fig. 20. Shear deformation envelopes of the shear links.

The cross-section of the DSCW piers is kept consistent as shown in Fig. 27.

$$V_{\mathrm{p}} = \frac{2M_{\mathrm{pn}}CR_{\mathrm{pn}}}{n_{\mathrm{F}}L_{\mathrm{w}}(1 - CR_{\mathrm{pn}})} \tag{9}$$

In this paper, the nominal plastic coupling ratio CR_{pn} is employed as the representative metric of the CR for executing parametric analysis. The CR_{pn} parameter consists of 11 different values ranging from 0.2 to 0.7 in intervals of 0.05 and is varied by changing the sectional details of the shear links. The shear demand of the shear links corresponding to a specific CR_{pn} can be determined by Eq. (9). The shear links are designed according to the code ANSI/AISC 360 [34], with shear span ratios $e/(M_{\mathrm{p}}/V_{\mathrm{p}})$ of approximately 0.8 and 1.1, where M_{p} refers to the full-section plastic bending strength. The elastic connecting beams are expected to retain elastic and are therefore designed to have bending and shear strengths exceeding twice the corresponding strengths of the shear links. The axial load ratio n is also considered as a key parameter with values between 0.3 to 0.6 in intervals of 0.1. To investigate the interactive influences between structural geometric characteristics and CR_{pn} on the yielding sequence, the models with different number of stories (7, 11, 18, and 30) are considered. The standard story height is

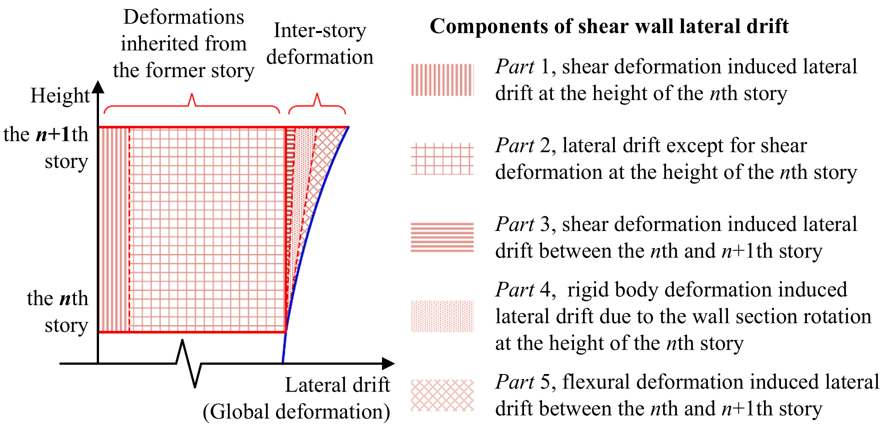

Fig. 21. Deformation mechanisms and composition of shear walls.

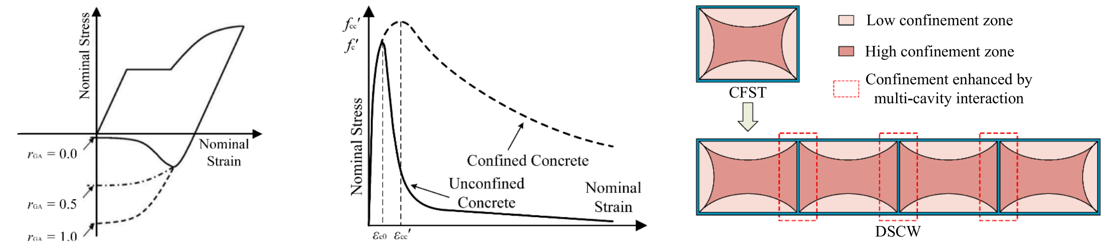

(a) Buckling behavior in RSMM (b) Mander’s confined concrete model (c) Muti-cavity interaction effect

Fig. 22. Schematic for steel and concrete material models.

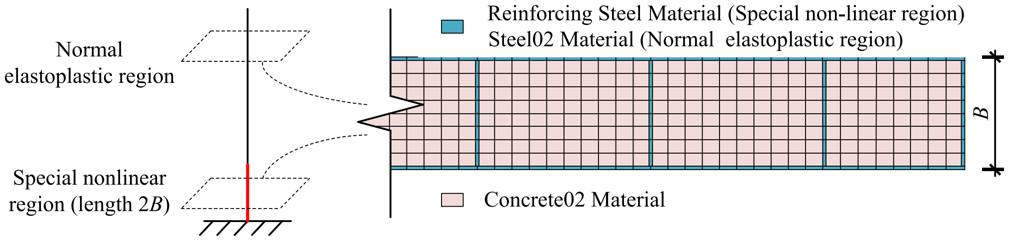

Fig. 23. Schematic for fiber-based beam-column element model for DSCW.

Table 3
Properties of the two-node link element for shear links.

Springs	Parameters	Formulas & values
Elastic axial spring	Axial stiffness K_a	$K_a=E_{CB}A_{CB}/e$
Non-linear shear spring	Elastic stiffness K_s	$K_s=[e^3/(12E_{CB}I_f)+e/G_{CB}A_w]^{-1}$
	Shear yield force V_p	$V_p=0.58f_{yw}A_w$
	Parameters that control the transition from elastic to plastic branch	$R_0=18.5$, $cR_1=0.9$, $cR_2=0.1$
	Kinematic hardening parameter b	$b=0.003$
	Isotropic hardening parameters a_1, a_2, a_3, a_4	$a_1=a_3=0.14$, $a_2=a_4=1.0$
Elastic flexural spring	Flexural stiffness K_f	$K_f=E_{CB}I_f/e$

3600 mm and the models with 7, 11, 18, and 30 stories correspond to structural aspect ratios λ of 4.2, 6.6, 10.8 and 18, respectively. The structural aspect ratios λ is defined as the ratio of structural global height to the distance between the center axes of the two DSCW piers, i.e., $\lambda=n_F h_F/L_W$. Two comparative models with 18 stories are set up with story heights of 2200 mm and 6000 mm, having the same total height and aspect ratio as the standard 11-story and 30-story models.

4.4. Parametric analysis results and discussion

Take the series models with $n_F=11$, $n=0.4$, and $\lambda=6.6$ as an example, the pushover curves are shown in Fig. 28, other numerical analysis results are summarized in Fig. A2 in the Appendix. The vertical coordinate of the curves is the lateral drift at the equivalent height h_{eq} of the C-DSCW model. The h_{eq} can be determined by the method of base shear

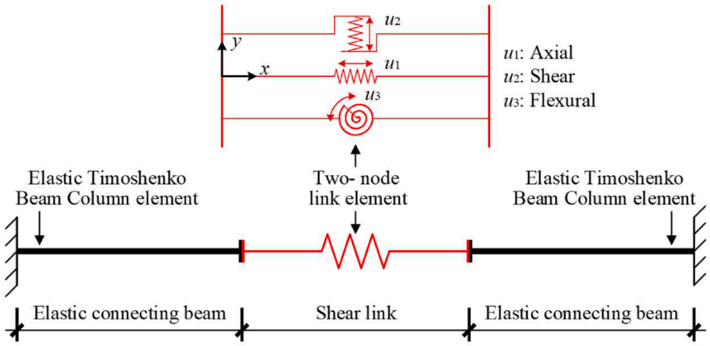

(a) Modeling of shear links and elastic connecting beams

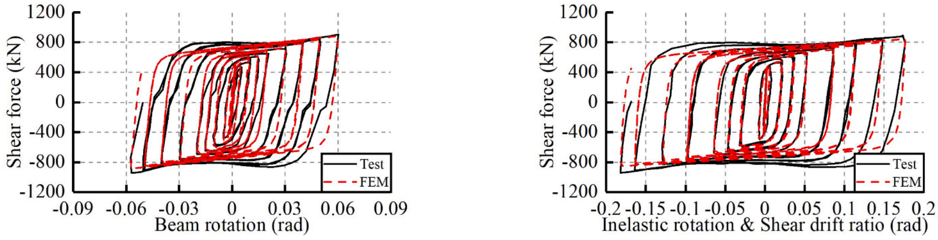

(b) Specimen CB-1 in [21]   (c) Shear link of specimen CB-1 in [21]

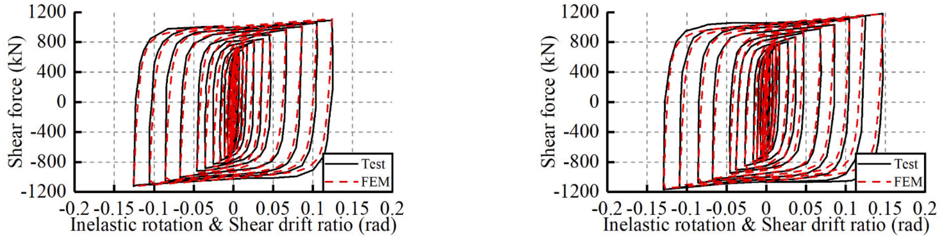

(d) Shear link Q11 in [22]   (e) Shear link Q21 in [22]

Fig. 24. Schematic and validation for modeling of shear links and elastic connecting beams.

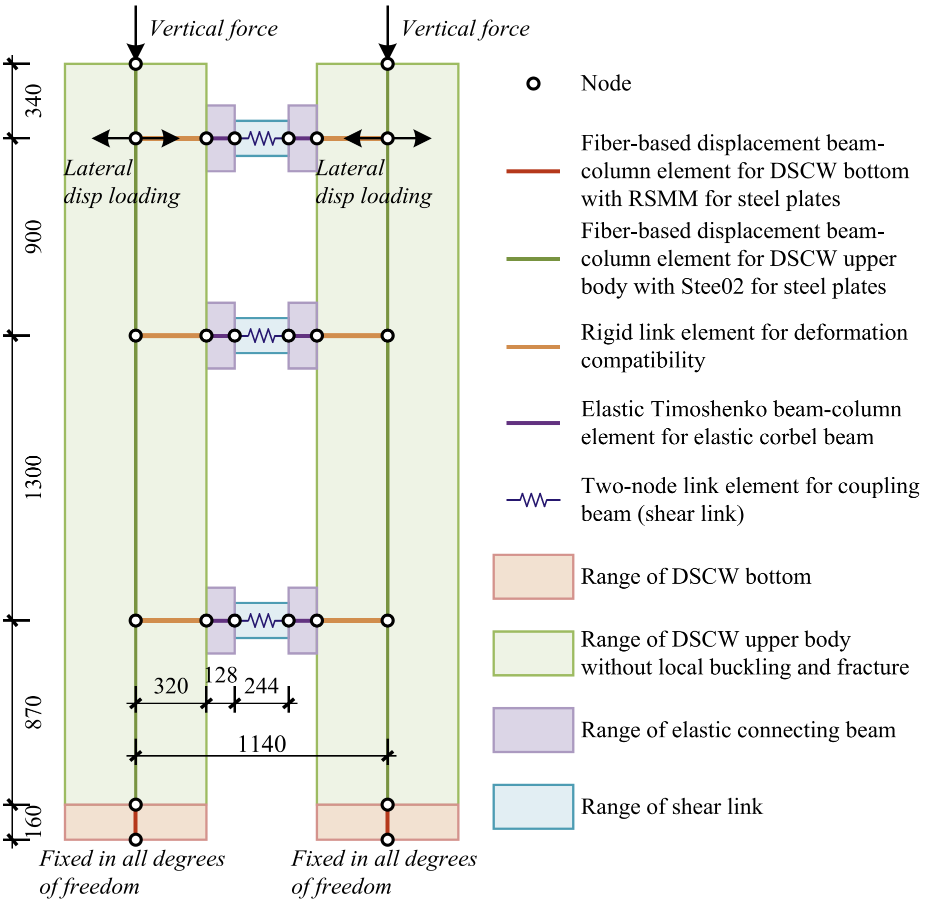

Fig. 25. Schematic for modeling of tested C-DSCW specimen.

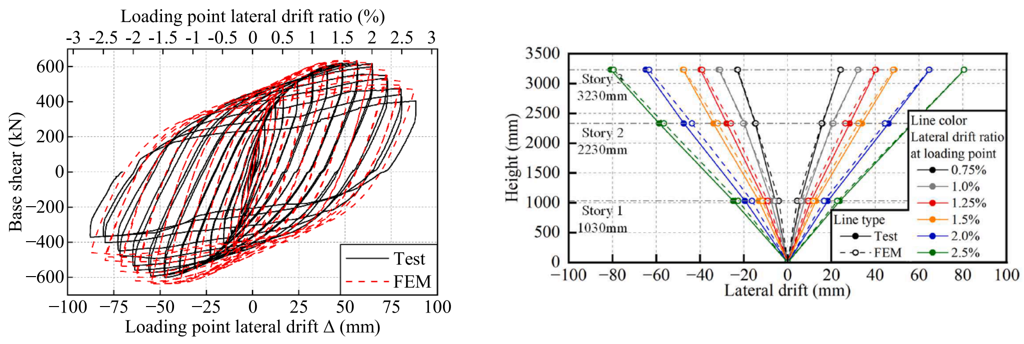

(a) Hysteresis curves

(b) Lateral deformation pattern

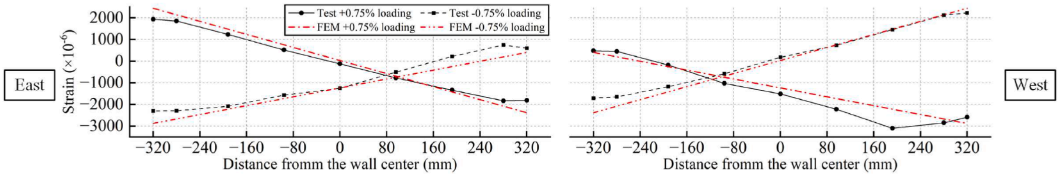

(c) Strain response envelopes of the cross-section at height of T1~T18 SGs

Fig. 26. Validation for modeling of C-DSCW specimen.

equivalence and base moment equivalence, as shown in Eq. (10), where h_i refers to the height from ground at the ith story.

$$h_{\mathrm{eq}} = \frac{\sum F_{\mathrm{m}i} h_i}{\sum F_{\mathrm{m}i}} \tag{10}$$

It can be concluded that increasing CR_{pn} can significantly improve the stiffness and lateral load-bearing capacity of the C-DSCW system. When the value of CR_{pn} is low, the coupling effect is insufficient to protect the wall piers. Conversely, a very high CR_{pn} value produces excessive additional axial forces, which can reduce the ductility of the

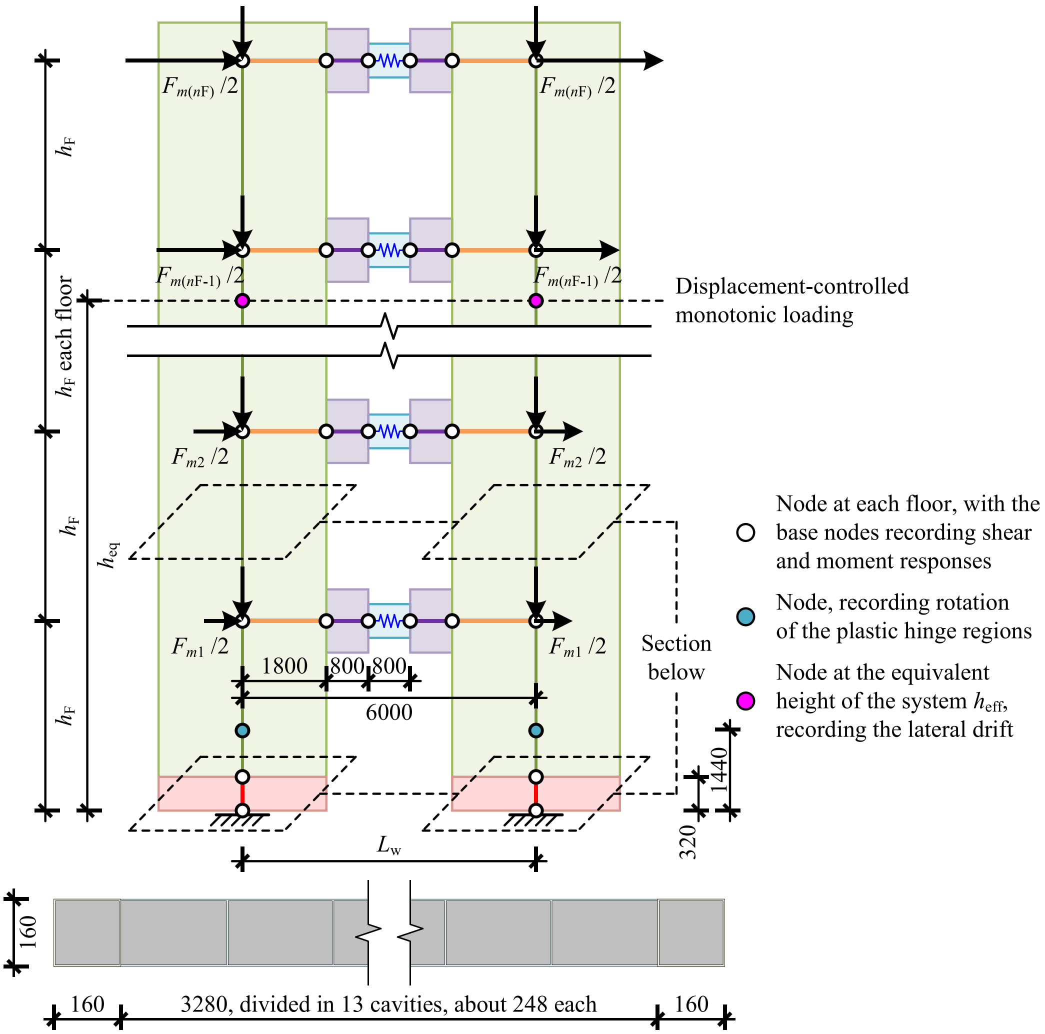

Fig. 27. Schematic for modeling of parametric analysis models.

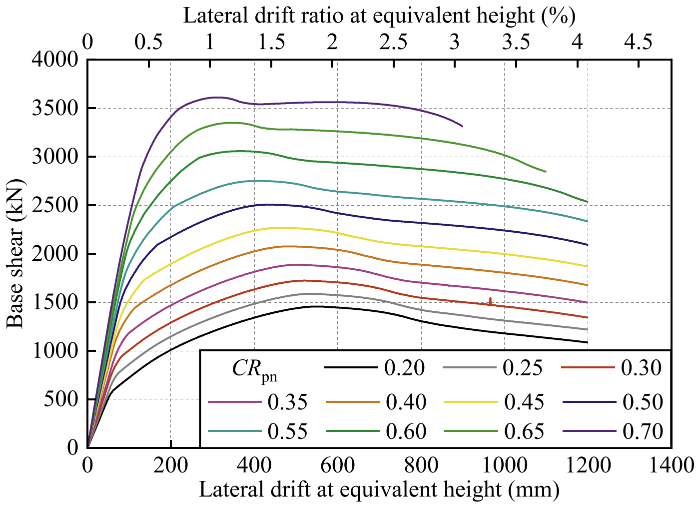

Fig. 28. Pushover results of models with n_F=11, n=0.4 and λ=6.6.

wall piers. For series specimens with n_F=30, a low CR_{pn} value will instead cause a more rapidly degrading branch in the pushover curve. This occurs even though the two DSCW piers do not exhibit plastic behavior and flexural failures. This reveals that the additional overturning moment generated by the gravity second-order effect becomes the main factor controlling the lateral resisting capacity of the high-rise coupled wall system. Thus, the high-rise structures are more suitable for high CR_{pn} to improve structural integrity. Within the range of studied parameter values, increasing the axial compression ratio n always leads to a degradation of the lateral strength and ductility of the C-DSCW system.

Take the model with n_F=11, n=0.4, λ=6.6 and CR_{pn}=0.40 as an example, Fig. 29(a) demonstrates the methodology to determine the yielding sequence of the DSCW piers and shear links. Where the DS_2 denotes the damage state in which a steel shear link needs to be repaired or replaced after fully undergoing plastic deformation and dissipating seismic energy. The criterion of DS_2 is that the steel shear link reaches a shear drift ratio of 0.06 rad, which corresponds to the median of the DS_2 fragility curve in the reference [63]. The initial yielding of the shear links refers to their shear internal force responses reaching V_p according to Eq. (8). The characteristic yielding behaviors of each component during the pushover process are marked in the legend. Fig. 29(b) demonstrates the methodology to determine the yield point of the DSCW piers, which is divided into two subplots. The two subplots Fig. 29(b) share a same horizontal coordinate, which is the average rotation in the plastic hinge regions of the two DSCW piers ($\theta_{w,avg}$). The vertical coordinates in the upper and lower subplots of Fig. 29(b) refer to the the summation of the base moment responses of the two DSCW piers and the lateral drift at h_{eq} (consistent with the horizontal coordinate in Fig. 29 (a)). The $\theta_{w,avg}$ can be obtained by outputting the rotation responses of the two DSCW piers at the reference nodes of the plastic hinge regions (shown in Fig 27) in the numerical models, and then taking the average of the rotation responses of the two DSCW piers. In this way, the yield point of the DSCWs can be determined from the moment-rotation curve based on the equivalent elasto-plastic energy method [64]. Based on this point, the corresponding lateral drift at h_{eq} of the C-DSCW system can be obtained (marked by black square), and thus the yield point of the DSCWs can be determined in the pushover curve.

To quantitatively and intuitively characterize the yielding sequence of the C-DSCW system, the indexes R_1 and R_2 are defined here. R_1 and R_2 respectively denote the proportion of shear links that initially yield and reach DS_2, at the time of the DSCW piers yielding [56]. The analytical results of the yielding sequence are displayed in Fig. 30. It can be concluded that n and CR_{pn} have a significant effect on the yielding sequence of the C-DSCW system. The models with different story numbers and the same structural height (i.e., structural aspect ratio λ) have very similar yielding sequences, which indicates the dimensionless parameter λ, rather than the story number or the story height, is another key factor influencing the yielding sequence of the C-DSCW system. High axial load ratio n, high nominal coupling ratio CR_{pn}, and low structural aspect ratio λ will make the DSCW piers tend to yielding earlier. Only extreme parameter values can lead to the DSCW piers yielding earlier than the initial yielding of the shear links.

In summary of the conclusions relating to the pushover curves and the yielding sequence analysis, the determination of nominal coupling ratio CR_{pn} in the capacity-based design of C-DSCW systems should follow the principles: To fully utilize the coupling effect, higher CR_{pn} values are recommended to be employed to improve the lateral stiffness and load-bearing capacity, while high R_1 and R_2 values should be ensured as a priority to control the yielding sequence. The recommended values of CR_{pn} considering the effects of structural aspect ratio λ and axial load ratio n are summarized in Table 4 and Fig. 31.

5. Conclusion

This paper presents an integrated experimental and numerical investigation on the seismic performance and yielding sequence of the C-DSCW system with replaceable steel shear links. The research conclusions are summarized as follows:

(1) An experimental study is conducted with a 3-story C-DSCW specimen under combined axial compression and horizontal cyclic loading. The tested results show that within 0.75% loading drift ratio, the DSCW piers can be restored almost to its original state by replacing the shear links. Furthermore, the test highlights the superior ductility and energy dissipation capacity of a properly designed C-DSCW system.

(2) The FEM for C-DSCW system is established by the OpenSEES platform. The proposed modeling method included DSCW piers and steel coupling beams at the component level, as well as the modeling and components' assembling approaches at the structural level. The reliability and accuracy of the models are verified based on the experimental results.

(3) A parametric analysis is conducted to explore the influence of the CR_{pn}, n, n_F, and λ on the yielding sequence of the C-DSCW system. The analytical results show that the coupling mechanism can effectively improve the lateral stiffness and load-bearing capacity of the C-DSCW system. The analysis also reveals that in the high-rise (large λ value) coupled wall system, the additional overturning moment generated by the gravity second-order effect becomes the main factor controlling its lateral resisting capacity. Thus, the integrity provided by the high CR_{pn} is particularly important in improving the performance of the system.

(4) Parameters n, CR_{pn}, and λ have a significant effect on the yielding sequence of the C-DSCW system. The high value of n, CR_{pn}, and low value of λ will make the DSCW piers tend to experience yielding earlier. Only extreme parameter values can lead to the DSCW piers yielding earlier than the initial yielding of the shear

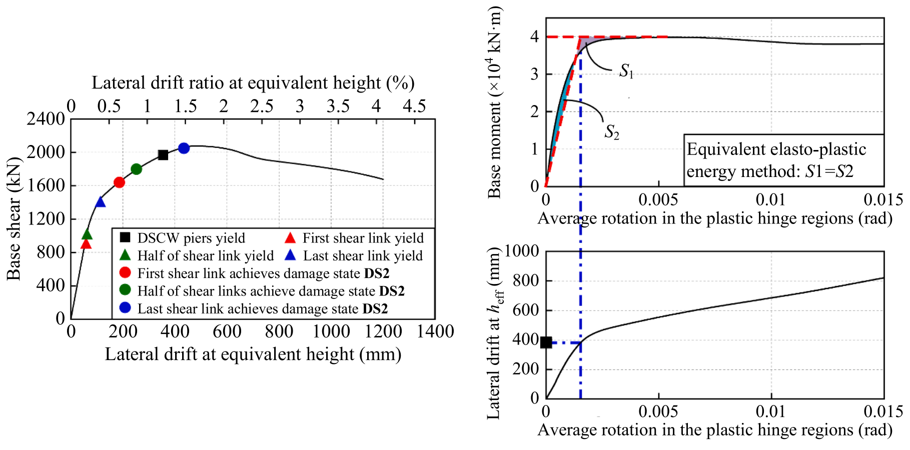

(a) Yielding sequence in pushover curve (b) Yield point for DSCW piers

Fig. 29. Schematic for determining the yielding sequence.

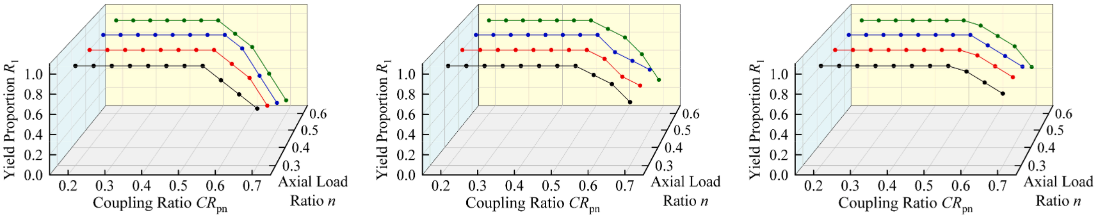

(a) R_1 (n_F=7, λ=4.2) (b) R_1 (n_F=11, λ=6.6) (c) R_1 (n_F=18, λ=10.8)

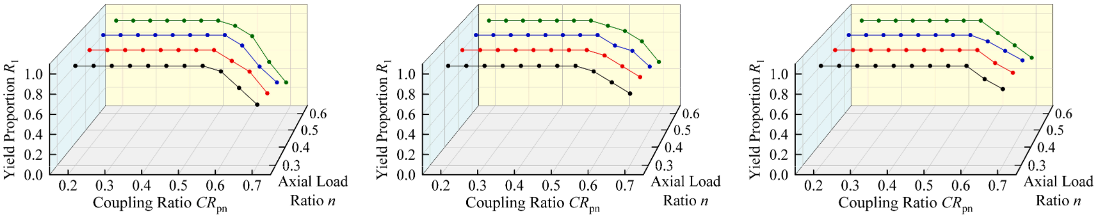

(d) R_1 (n_F=18, λ=6.6) (e) R_1 (n_F=18, λ=18) (f) R_1 (n_F=30, λ=18)

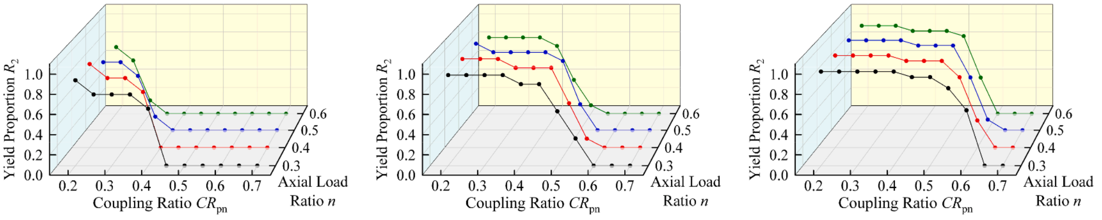

(g) R_2 (n_F=7, λ=4.2) (h) R_2 (n_F=11, λ=6.6) (i) R_2 (n_F=18, λ=10.8)

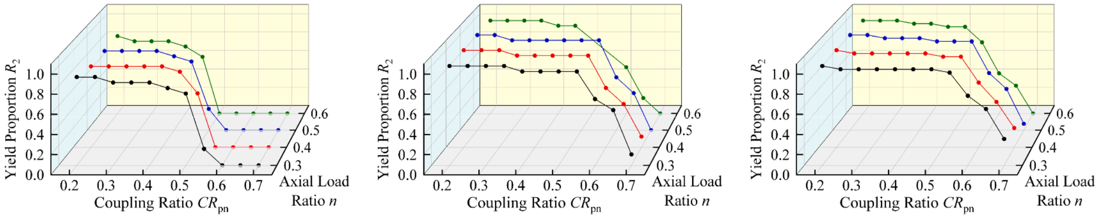

(j) R_2 (n_F=18, λ=6.6) (k) R_2 (n_F=18, λ=18) (l) R_2 (n_F=30, λ=18)

Fig. 30. Yielding sequence of the DSCW piers and shear links.

Table 4
Relationship between recommended CR_{pn} and structural parameters.

Recommended CR_{pn}		Axial load ratio n			
		0.3	0.4	0.5	0.6
Structural aspect ratio λ	4.2	0.40	0.35	0.30	0.25
	6.6	0.50	0.45	0.45	0.40
	10.8	0.60	0.55	0.55	0.50
	18.0	0.65	0.60	0.60	0.55

links. Based on the parametric analysis results, the recommended values of the CR_{pn} considering the interactive influences of other structural parameters are provided.

CRediT authorship contribution statement

Haowen Hou: Writing – original draft, Visualization, Validation, Software, Methodology, Investigation, Formal analysis, Data curation, Conceptualization. **Wei Wang:** Writing – review & editing, Supervision, Resources, Project administration, Methodology, Investigation, Funding acquisition, Conceptualization. **M. Shahria Alam:** Writing – review & editing, Validation, Supervision, Methodology, Investigation, Conceptualization. **Shiye Wang:** Writing – review & editing, Validation, Methodology, Investigation. **Jiajun Du:** Validation, Software, Investigation, Data curation.

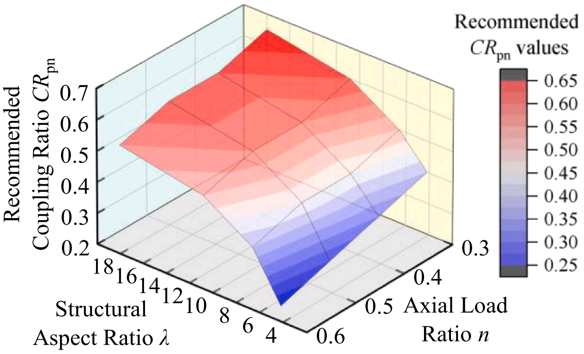

Fig. 31. Relationship between recommended CR_{pn} and structural parameters.

Declaration of competing interest

The authors declare that they have no known competing financial interests or personal relationships that could have appeared to influence the work reported in this paper.

Acknowledgments

The financial supports from the National Natural Science Foundation of China (NSFC) with Grant No. 52378182, the Collaborative Research Project under the International Joint Research Laboratory of Earthquake Engineering at Tongji University, the Shanghai 2022 Science and Technology Innovation Action Plan Social Development Science and Technology Research Project with Grant No. 22dz1201700, and International Exchange Program for Graduate Students of Tongji University are gratefully acknowledged.

Appendix

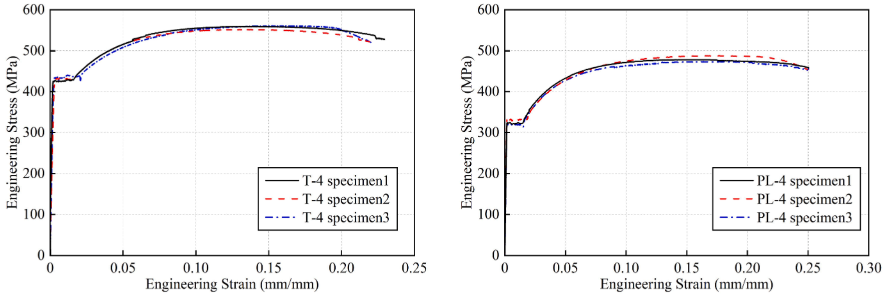

(a) T-4

(b) PL-4

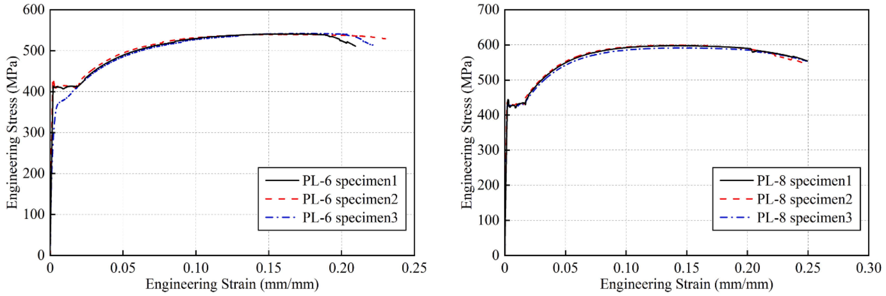

(c) PL-6

(d) PL-8

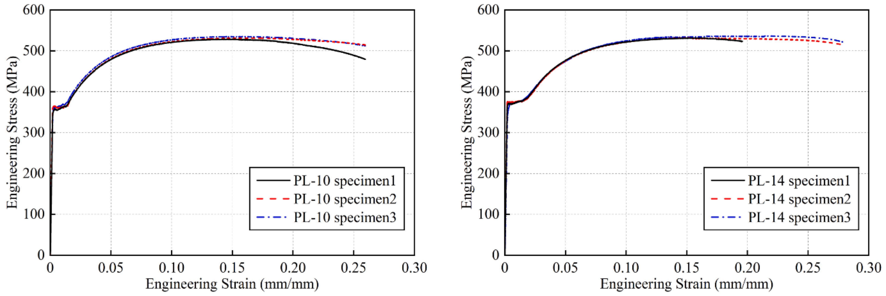

(e) PL-10

(f) PL-14

Fig. A1. Strain-Stress responses of steel coupons.

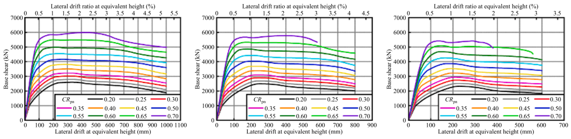

(a) n_F=7, n=0.3, λ=4.2 (b) n_F=7, n=0.4, λ=4.2 (c) n_F=7, n=0.5, λ=4.2

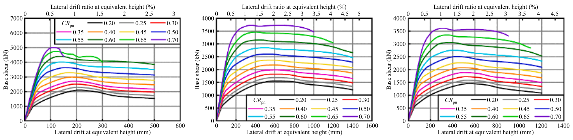

(d) n_F=7, n=0.6, λ=4.2 (e) n_F=11, n=0.3, λ=6.6 (f) n_F=11, n=0.4, λ=6.6

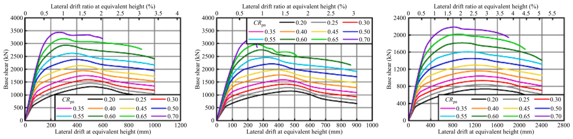

(g) n_F=11, n=0.5, λ=6.6 (h) n_F=11, n=0.6, λ=6.6 (i) n_F=18, n=0.3, λ=10.8

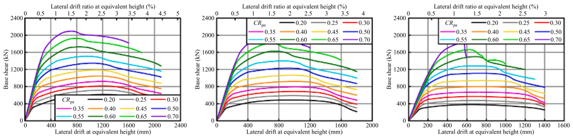

(j) n_F=18, n=0.4, λ=10.8 (k) n_F=18, n=0.5, λ=10.8 (l) n_F=18, n=0.6, λ=10.8

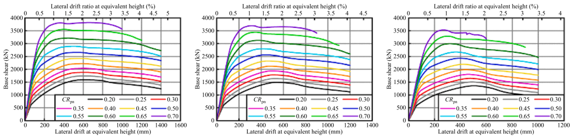

(m) n_F=18, n=0.3, λ=6.6 (n) n_F=18, n=0.4, λ=6.6 (o) n_F=18, n=0.5, λ=6.6

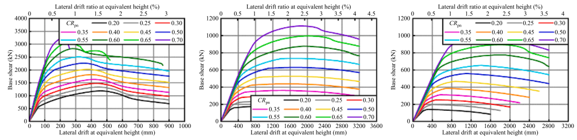

(p) n_F=18, n=0.6, λ=6.6 (q) n_F=18, n=0.3, λ=18 (r) n_F=18, n=0.4, λ=18

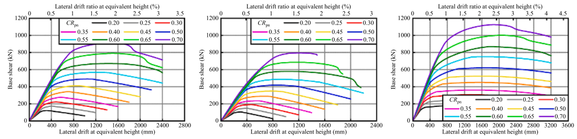

(s) n_F=18, n=0.5, λ=18 (t) n_F=18, n=0.6, λ=18 (u) n_F=30, n=0.3, λ=18

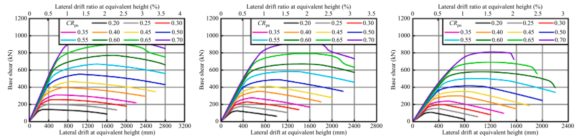

(v) n_F=30, n=0.4, λ=18 (w) n_F=30, n=0.5, λ=18 (x) n_F=30, n=0.6, λ=18

Fig. A2. Pushover results of all parametric analysis models.

Data availability

Data will be made available on request.

References

[1] S. El-Tawil, K.A. Harries, P.J. Fortney, B.M. Shahrooz, Y. Kurama, Seismic design of hybrid coupled wall systems: state of the art, J. Struct. Eng. 136 (7) (2010) 755–769.

[2] S. El-Tawil, P. Fortney, K. Harries, B.M. Shahrooz, Y. Kurama, X. Tong, Recommendations for Seismic Design of Hybrid Coupled Wall Systems, American Society of Civil Engineers, 2009.

[3] T. Paulay, Coupling beams of reinforced concrete shear walls, J. Struct. Divis. 97 (3) (1971) 843–862.

[4] S. El-Tawil, C.M. Kuenzli, M. Hassan, Pushover of hybrid coupled walls. I: design and modeling, J. Struct. Eng. 128 (10) (2002) 1272–1281.

[5] S. El-Tawil, C.M. Kuenzli, Pushover of hybrid coupled walls. II: analysis and behavior, J. Struct. Eng. 128 (10) (2002) 1282–1289.

[6] J.D. Aristizabal-Ocfaoa, Seismic behavior of slender coupled wall systems, J. Struct. Eng. 113 (10) (1987) 2221–2234.

[7] Y. Wu, Q. Zhou, Y. Su, B. Wang, Seismic design method and experimental study of composite steel plate-concrete coupled wall systems, J. Build. Struct. 38 (S1) (2017) 58–65. Chinese.

[8] Q. Zhou, M. Su, Y. Shi, L. Guan, M. Lian, L. Jiang, Y. Yang, L. Zhang, Hysteretic behavior of the hybrid coupled partially encased composite wall system, Structures 34 (2021) 4216–4236.

[9] Y. Sun, Study on Seismic Behavior of Hybrid Coupled Wall with Replaceable Steel Coupling Beams, TsingHua University: Beijing, China, 2015.

[10] Building Code Requirements for Structural Concrete and Commentary, ACI 318-14, American Concrete Institute (ACI): Farmington Hills, MI, USA, 2014.

[11] K.A. Harries, B. Gong, B.M. Shahrooz, Behavior and design of reinforced concrete, steel, and steel-concrete coupling beams, Earthq. Spectra 16 (4) (2000) 775–799.

[12] L. Galano, A. Vignoli, Seismic behavior of short coupling beams with different reinforcement layouts, ACI Struct. J. 97 (6) (2000) 876–885.

[13] K.A. Harries, B.M. Shahrooz, Hybrid coupled wall systems, Concret. Int. 27 (5) (2005) 45–51.

[14] P.J. Fortney, B.M. Shahrooz, G.A. Rassati, Large-scale testing of a replaceable "fuse" steel coupling beam, J. Struct. Eng. 133 (12) (2007) 1801–1807.

[15] K.A. Harries, B. Gong, B.M. Shahrooz, Behavior and design of reinforced concrete, steel, and steel-concrete coupling beams, Earthq. Spectra 16 (4) (2000) 775–799.

[16] J. Nie, H. Hu, M.R. Eatherton, Concrete filled steel plate composite coupling beams: experimental study, J. Construct. Steel Res. 94 (2014) 49–63.

[17] J.O. Malley, E.P. Popov, Shear links in eccentrically braced frames, J. Struct. Eng. 110 (9) (1984) 2275–2295.

[18] N. Mansour, C. Christopoulos, R. Tremblay, Experimental validation of replaceable shear links for eccentrically braced steel frames, J. Struct. Eng. 137 (10) (2011) 1141–1152.

[19] National Research Council, National Earthquake Resilience: Research, Implementation, and Outreach, The National Academies Press, Washington DC, 2011.

[20] C. Fang, W. Wang, C. Qiu, S. Hu, G.A. MacRae, M.R. Eatherton, Seismic resilient steel structures: a review of research, practice, challenges and opportunities, J. Construct. Steel Res. 191 (2022) 107172.

[21] X. Ji, Y. Wang, Q. Ma, T. Okazaki, Cyclic behavior of replaceable steel coupling beams, J. Struct. Eng. 143 (2) (2017) 04016169.

[22] X. Ji, Y. Wang, Q. Ma, T. Okazaki, Cyclic behavior of very short steel shear links, J. Struct. Eng. 142 (2) (2016) 04015114.

[23] J. Yu, L. Xu, C. Zhao, X. Feng, Mechanical performance study of coupled partially encased composite shear walls with double replaceable fuse components, Structures 59 (2024) 105748.

[24] J. Yan, J. Fan, R. Ding, X. Nie, Steel-concrete-steel sandwich composite structures: a review, Eng. Struct. 302 (1) (2024) 117449.

[25] S. Wang, W. Wang, Y. Chen, H. Hou, S. Xie, Seismic performance of double skin composite wall under maximum considered far-field earthquake loading protocol, J. Build. Eng. 55 (2022) 104705.

[26] S. Shafaei, A.H. Varma, J. Seo, R. Klemencic, Cyclic lateral loading behavior of composite plate shear walls/concrete filled, J. Struct. Eng. 147 (10) (2021) 04021145.

[27] H. Hou, W. Wang, S. Wang, Seismic damage assessment for flexural double skin composite walls based on the modified Park-Ang model, Thin-Wall. Struct. 196 (2023) 111445.

[28] X. Ji, M. Xu, Y. Zhuang, Z. Jiang, Fragility curves of reinforced concrete shear walls and coupling beams, Eng. Mech. 37 (4) (2020) 205–216. Chinese.

[29] T.S. Eom, H.G. Park, C.H. Lee, J.H. Kim, I.H. Chang, Behavior of double skin composite wall subjected to in-plane cyclic loading, J. Struct. Eng. 135 (10) (2009) 1239–1249.

[30] D. Xu, J. Wang, B. Xiang, J. Yan, T. Wang, Behavior of double skin composite core wall subject to biaxial cyclic loads, Eng. Struct. 279 (2023) 115591.

[31] D. Xu, Y. Cui, J. Yan, B. Xiang, H. Liu, Y. Lei, T. Wang, Cyclic test evaluation of double skin composite hybrid coupled wall with frictional steel truss coupling beams, J. Build. Eng. 79 (2023) 107832.

[32] M. Broberg, S. Shafaei, E. Kizilarslan, J. Seo, A.H. Varma, M. Bruneau, R. Klemencic, Capacity design of coupled composite plate shear wall-concrete-filled system, J. Struct. Eng. 148 (4) (2021) 04022022.

[33] Seismic Provision for Structural Steel Buildings, ANSI/AISC 341-16, American Institute of Steel Construction (AISC), Chicago, IL, USA, 2016.

[34] Specification for Structural Steel Buildings, ANSI/AISC 360-16, American Institute of Steel Construction (AISC), Chicago, IL, USA, 2016.

[35] Technical specification for steel tube-reinforced concrete column structures, T/CECS 188-2019, China Architecture & Building Press, Beijing, China, 2019. in Chinese.

[36] H. Hou, W. Wang, Y. Chen, An assembled beam-to-double skin composite wall joint with insert diaphragm: configuration, experiment, mechanical model and design method, J. Build. Eng. 74 (2023) 106883.

[37] Metallic Materials - Tensile Testing - Part 1: Method of Test at Room Temperature, GB/T 228.1-2010, Standards Press of China, Beijing, China, 2011. Chinese.

[38] A.M. Neville, A general relation for strengths of concrete specimens of different shapes and sizes, ACI J. Proceed. 63 (10) (1966) 1095–1110.

[39] Interim Testing Protocols for Determining the Seismic Performance Characteristics of Structural and Nonstructural Components, FEMA 461, Federal Emergency Management Agency (FEMA), Washington DC, USA, 2007.

[40] Q. Cheng, M. Su, M. Lian, H. Zhang, B. Guan, Cyclic behavior of high-strength steel framed-tube structures with bolted replaceable shear links, Eng. Struct. 210 (2020) 110395.

[41] P. Feng, S. Cheng, Y. Bai, L. Ye, Mechanical behavior of concrete-filled square steel tube with FRP-confined concrete core subjected to axial compression, Compos. Struct. 123 (2015) 312–324.

[42] Y. Alzeni, M. Bruneau, In-plane cyclic testing of concrete-filled sandwich steel panel walls with and without boundary elements, J. Struct. Eng. 143 (9) (2017) 04017115.

[43] S. Shafaei, A.H. Varma, D. Huber, R. Klemencic, Lateral load behavior of C-PSW/CFs using steel members as boundary elements, J. Struct. Eng. 149 (9) (2023) 04023112.

[44] C. Xiong, X. Lu, X. Lin, Damage assessment of shear wall components for RC frame-shear wall buildings using story curvature as engineering demand parameter, Eng. Struct. 189 (2019) 77–88.

[45] J. Ji, A.S. Elnasha, D.A. Kuchma, Seismic fragility relationships of reinforced concrete high-rise buildings, Struct. Des. Tall Spec. Build. 18 (2009) 259–277.

[46] F. McKenna, G.L. Fenves, M.H. Scott, Open System for Earthquake Engineering Simulation, University of California, Berkeley, CA, USA, 2000.

[47] S.K. Kunnath, Y. Heo, M.ohleJ.F. Nonlinear, Uniaxial material model for reinforcing steel bars, J. Struct. Eng. 135 (4) (2009) 335–343.

[48] J.B. Mander, M.J. Priestley, R. Park, Theoretical stress-strain model for confined concrete, J. Struct. Eng. 114 (8) (1988) 1804–1826.

[49] H. Hou, W. Wang, S. Wang, Nonlinear modeling methods for cyclic analysis of double-skin composite shear walls, Thin-Wall. Struct. 187 (2023) 110737.

[50] X. Ji, D. Liu, Y. Sun, C.M. Hutt, Seismic performance assessment of a hybrid coupled wall system with replaceable steel coupling beams versus traditional RC coupling beams, Earthq. Eng. Struct. Dyn. 46 (4) (2017) 517–535.

[51] P. Dusicka, A.M. Itani, I.G. Buckle, Cyclic response of plate steels under large inelastic strains, J. Construct. Steel Res. 63 (2) (2007) 156–164.

[52] Y. Shi, M. Wang, Y. Wang, Experimental study of structural steel constitutive relationship under cyclic loading, J. Build. Mater. 15 (3) (2012) 293–300. Chinese.

[53] Technical Code for Steel Structure of Light-Weight Building with Gabled Frames, GB 51022-2015, China Architecture & Building Press, Beijing, China, 2015. Chinese.

[54] K.A. Harries, J.D. Moulton, R.L. Clemson, Parametric study of coupled wall behavior-implications for the design of coupling beams, J. Struct. Eng. 130 (3) (2004) 480–488.

[55] B.T. Teweldebrhan, S. Tesfamariam, Performance-based design of tall-coupled cross-laminated timber wall building, Earthq. Eng. Struct. Dyn. 51 (7) (2022) 1677–1696.

[56] C.C. Hung, W.T. Lu, Towards achieving the desired seismic performance for hybrid coupled structural walls, Earthq. Struct. 9 (6) (2015) 1251–1272.

[57] M. Cheng, R.ijalul Fikri, C. Chen, Experimental study of reinforced concrete and hybrid coupled shear wall systems, Eng. Struct. 82 (2015) 214–225.

[58] X. Cheng, C. Lu, X. Ji, Y. Li, Y. Song, Seismic behavior of reinforced concrete slender walls subjected to variable axial loads, Soil Dyn. Earthq. Eng. 175 (2023) 108253.

[59] J. Shi, L. Guo, B. Qu, In-plane cyclic tests of double-skin composite walls with concrete-filled steel tube boundary elements, Eng. Struct. 250 (2022) 113301.

[60] S. Huang, Y. Huang, A. He, X. Tang, Q. Chen, X. Liu, J. Cai, Experimental study on seismic behavior of an innovative composite shear wall, J. Construct. Steel Res. 148 (2018) 165–179.

[61] Y. Wang, L. Guo, H. Li, S. Shafaei, Y. Yu, Lateral load response of L-shaped steel–concrete composite shear walls using multi-partition steel tube, Eng. Struct. 293 (2023) 116671.

[62] D. Pennucci, T.J. Sullivan, G.M. Calvi, Inelastic higher-mode response in reinforced concrete wall structures, Earthq. Spectra 31 (3) (2015) 1493–1514.

[63] C.K. Gulec, B. Gibbons, A. Chen, A.S. Whittaker, Damage states and fragility functions for link beams in eccentrically braced frames, J. Construct. Steel Res. 67 (9) (2011) 1299–1309.

[64] R. Park, State of the art report ductility evaluation from laboratory and analytical testing, in: Proceedings of Ninth World Conference on Earthquake Engineering, Tokyo, Kyoto, Japan, 1988, pp. 605–616.